A flow-curvature-based model for channel meandering in tidal marshes

Giulio Mariotti[1,2] and Alvise Finotello[3]

[1]Department of Oceanography and Coastal Sciences, Louisiana State University, Baton Rouge, LA, USA

[2]Center for Computation and Technology, Louisiana State University, Baton Rouge, LA, USA

[3]Department of Geosciences, University of Padova, Padova, Italy.

Corresponding author: Giulio Mariotti (gmariotti@lsu.edu)

Key Points:

- Novel, depth-averaged, Cartesian-grid-based numerical model to simulate channel meandering in tidal marshes
- Realistic channel morphologies and dynamics are reproduced, including cuspate bends, meander cutoffs, and channel piracies
- Model simulates the ecomorphodynamic evolution of tidal marshes with branching and meandering channel networks over decades to millennia

Keywords

Tidal marshes, Tidal Meanders, Channel Migration, Ecomorphodynamics, Numerical Modelling

Abstract

Channel meandering is ubiquitous in tidal marshes, yet it is routinely omitted in morphodynamic models. Here we propose a novel numerical method to simulate channel meandering in tidal marshes on a Cartesian grid. The method calculates a first-order flow by considering the balance between pressure gradient and bed friction. To account for flow momentum shift towards meander outer banks, the flow is empirically modified. Unlike previous simplified methods that relied on the curvature of the bank, this modification is based on the curvature of the flow, making the model suitable for use in dendritic channel networks. The modified flow intrinsically accounts for the topographic steering effect, which tends to deflect the momentum toward the outer bank. As a result, the outer bank becomes steeper and erodes due to soil creep. Additionally, the outer bank experiences erosion proportional to the flow curvature. This erosion mechanism parameterizes the direct erosion caused by flow impacting the bank through a proportionality coefficient, which modulates the rate of lateral channel migration. Deposition on the inner bank is automatically simulated by the model, triggered by reduced bed shear stress in that area. The model accurately reproduces meander sinuosity, migration rates, and associated processes such as cutoffs, channel piracies, and network reorganizations. The model provides an efficient tool for predicting marsh landscape evolution from decades to millennia, which will enable exploring how lateral migration and meandering of tidal channels affect marsh ecomorphodynamics, carbon and nutrient cycling, drainage efficiency, and pond dynamics.

1 Introduction

Branching and meandering tidal channel networks are widespread in low-lying coastal areas, from open coasts to back-barrier lagoons, as well as in tidally-influenced fluvio-deltaic and estuarine plains (Fagherazzi et al., 1999; Kearney and Fagherazzi, 2016; Rinaldo et al., 1999a, 1999b) (Fig. 1). Besides governing tide propagation, thereby mediating changes in local mean sea level and tidal range, tidal channel networks control the ecomorphodynamic evolution of the wetlands they drain by regulating fluxes of water, sediments, nutrients, pollutants, and particulate matter (Coco et al., 2013; Hughes, 2012; Marani et al., 2003). Given their importance, there is a pressing need to understand the formation and evolution of these landscape features, especially when considering climatic changes and anthropogenic disturbances (Stefanon et al., 2012; Zhou et al., 2014a). Even though some major progress has occurred over the last two decades in terms of numerical modeling and laboratory experiments, the long-term prediction of tidal channel network morphological evolution remains a major challenge both at the theoretical and practical levels (Belliard et al., 2015; Belliard, 2014; Cleveringa and Oost, 1999; Cosma et al., 2020; Geng et al., 2020; Hood, 2014; Kleinhans et al., 2015; Stefanon et al., 2012; Xu et al., 2017; Zhou et al., 2014b).

A major limitation in understanding the long-term evolution of tidal marshes has been the widely accepted notion that tidal channel networks are stable, poorly dynamic geomorphological features (Choi and Jo, 2015; Fagherazzi et al., 2004; Gabet, 1998; Garofalo, 1980; Kleinhans et al., 2009). This notion caused the dynamics of mature networks to be largely disregarded in conventional ecogeomorphological practices, projections of local sea-level changes, and estimates of biogeochemical fluxes in highly-productive tidal wetland ecosystems. Although channel network ontogeny occurs on timescales considerably shorter than those involved in other relevant ecomorphodynamic processes such as sea-level changes and vegetation dynamics (D'Alpaos et

al., 2005; Fagherazzi and Sun, 2004; Kirwan and Murray, 2007), field observations have shown that channels are highly dynamic systems that can change over decadal timescales (Rizzetto and Tosi, 2012; Shimozono et al., 2019; Wilson et al., 2017).

Recent research provided proof of concept that tidal channel lateral migration and adjustment to changing external forcings are key, yet largely unexplored, drivers for marsh morphodynamics (Cosma et al., 2019, 2020; Finotello et al., 2018, 2019a, 2020c, 2020b). In particular, channel meandering, coupled with the characteristically high drainage density of channel networks, is likely to produce frequent piracies and network reorganizations (Cosma et al., 2020; Letzsch and Frey, 1980; Litwin et al., 2013). These changes drive profound modifications of hydrological connectivity, thus ultimately affecting the morphology, sedimentology, ecology, and carbon storage capacity of the marsh system. For instance, the continued reworking of tidal channel banks is likely to have important effects on vegetation dynamics and blue carbon fluxes because it removes established vegetation along the channel margins and allows the process of ecological succession to begin anew; moreover, it exposes organic-rich substrates, thereby affecting carbon fluxes (Elsey-Quirk et al., 2019; Hopkinson et al., 2018; Kalra et al., 2021; Leonardi et al., 2016). Meandering is also important from sedimentological perspectives since tidal channels are typically preserved in the sedimentary record through both laterally accreting deposits, which occur mostly at meander bends, and channel infilling as the tidal prism decreases when the channel is partially abandoned via either avulsion or meander cutoff (Brivio et al., 2016; Cosma et al., 2019, 2020).

In spite of its prominence and widespread occurrence, meandering in tidal channels lacks the detailed inspection that has been devoted to their fluvial relatives (Güneralp et al., 2012; Hooke, 2013; Ikeda et al., 1981; Leopold and Wolman, 1960; Parker et al., 1982). Of the various numerical models employed to reproduce the planimetric development of tidal channel networks (e.g., D'Alpaos et al., 2005; Fagherazzi and Sun, 2004; Kirwan and Murray, 2007; Van Maanen et al., 2013), none has insofar accounted for meander bend evolution. Numerical models have been proposed to simulate the evolution of individual, single-thread, sinuous tidal channels, assuming that a closed morphodynamic similarity exists between tidal and fluvial meanders. Hence, some authors directly employed modified versions of meandering-river centerline-migration models (e.g., Coulthard and Van De Wiel, 2012; Howard and Knutson, 1984; Ikeda et al., 1981; Nicholas, 2013; Seminara et al., 2001; Zolezzi and Seminara, 2001) to investigate the evolution of tidal meandering channels under the influence of changing tidal asymmetry (Fagherazzi et al., 2004) and in highly cohesive mudflat environments (Kleinhans et al., 2009). Solari et al. (2002) developed the only existing numerical model capable of forecasting the flow patterns and bed topography in mildly sinuous tidal channels through the implementation of linear stability theory derived for meandering rivers.

Despite their appeal, river meander models have major limitations when applied to tidal channels. First, river meander models are typically not able to simulate 2D cartesian domains, i.e., a gridded-based domain, which is generally the structure of salt-marsh ecomorphodynamic models (e.g., Belliard et al., 2015; D'Alpaos et al., 2007; Kirwan and Murray, 2007; Mariotti, 2020). Second, meandering tidal channels do not occur as isolated single-thread streams that freely wander through an otherwise empty alluvial plain. Rather, they are found within morphologically complex tidal channel networks where lateral channel migration leads to interactions with neighboring channels, producing frequent reorganization of the whole network structure and the formation of multichannel loops (e.g., Konkol et al., 2022) in addition to the classic meander neck

cutoffs observed in rivers. Third, tidal channels are characterized by highly variable widths due to channel funneling (Lanzoni and D'Alpaos, 2015), a phenomenon that can be disregarded when dealing with meandering rivers, which display limited width variations along their courses (Finotello et al., 2020a). Finally, in contrast to coastal wetlands, where sediments are predominantly fine and cohesive, conventional river meander models consider coarse non-cohesive sediments (e.g., Bogoni et al., 2017).

Here we propose a novel, computationally efficient numerical model capable of reproducing channel migration in tidal marshes and, more generally, the free evolution of tidal channel networks (i.e., including cutoffs and piracies). The model is informed and developed based on available field data and can simulate the evolution of salt-marsh landscapes on time scales ranging from decades to millennia.

2 Materials and Methods

2.1 MarshMorpho2D

Meandering in tidal channels was simulated using MarshMorpho2D, a numerically-efficient marsh evolution model that includes a variety of hydrodynamic and sedimentary processes. A summary of its components is reported below, and more details can be found in previous publications (Mariotti, 2020; Mariotti et al., 2016, 2019).

The model calculates a base tidal flow velocity field $\boldsymbol{U} = (U_x, U_y)$, representative of half a tidal cycle (i.e., either the ebb or flood phase), based on a balance between pressure gradient and linearized bed friction, and considering a tide-averaged water depth h for each cell (Mariotti, 2018, 2020):

$$\nabla \cdot (h\boldsymbol{U}) = S \tag{1}$$

$$\boldsymbol{U} \propto \frac{h^{4/3}}{n^2} \nabla \eta \tag{2}$$

The term η denotes the elevation of the free surface, whereas S is the source term for the tidal prism, and it is equal to $r/2 - \max(-r/2, \min(z, r/2))]/(T/2)$, where z is the bed elevation, r is the tidal range, and T is the tidal period. For numerical stability reasons, the minimum water depth is set equal to h=1 cm.

Sediment, which is here assumed to be only comprised of mud, can be resuspended from the bottom by both tidal currents and wind waves. Tidal velocities are used to estimate tidal dispersion (Di Silvio et al., 2010), which is employed to transport sediment in suspension. A constant baseline sediment diffusivity, equal to 10 m^2/s, is also included to account for all transport processes not directly simulated, such as wind-driven currents (by local forcings), wave-driven currents, shear-induced dispersion, and turbulent mixing.

Soil creep (i.e., gravity-driven diffusion of the elevation) is used to simulate marsh bank erosion (Mariotti et al., 2016, 2019). The creep coefficient is set equal to 0.1 m^2/yr and 3 m^2/yr in vegetated and unvegetated areas, respectively. Soil creep at the marsh banks (i.e., the interface between vegetated and unvegetated cells) is treated in a special way, given that bank erosion is driven by a complex interplay of hydrodynamic and geotechnical processes, and because its implementation is highly sensitive to the resolution of the computation (dx). Specifically, the constant diffusion term at the bank is set equal to $0.05dx$ ([m^2/yr], with dx in [m]), and an additional transport term is set proportional to the velocity at the bank and equal to $0.2dx|\boldsymbol{U}|$

([m^2/yr], with *dx* in meters). Overall, the interplay of these downslope transport mechanisms determines the shape of the channel cross-section and the related width-to-depth ratio.

Marsh vegetation is modeled as a function of the hydroperiod, which in turn is a function of bed elevation and tidal fluctuations. The upper limit for vegetation growth is set equal to the monthly median high water level, which depends on both the astronomic and the meteorological tides (Mariotti and Zapp, 2022). In addition to modifying soil creep (as described above), vegetation also modifies the bed drag, which in turn affects the flow. Specifically, Manning's friction coefficient is set equal to 0.02 $s/m^{1/3}$ and 0.1 $s/m^{1/3}$ in unvegetated and vegetated areas, respectively. Vegetation also drives in situ organic accretion, which is modeled as a parabolic function of elevation (Mariotti and Zapp, 2022; Morris et al., 2002), with a maximum accretion rate set equal to 5 mm/yr.

Settling velocity is equal to 0.2 mm/s in both the vegetated and unvegetated areas since net sediment deposition on the marsh is already triggered by the reduction in bed shear stress. This low value of settling velocity on the marsh platform is consistent with field estimates (Duvall et al., 2019; Lacy et al., 2020). Critical shear stress (τ_{cr}) for bed sediment erosion is assumed to be equal to 0.2 Pa for both unvegetated and vegetated areas to enable channel incision on the marsh platform. Yet, even with a relatively low value of marsh τ_{cr}, unchanneled flow is not able to induce marsh erosion, which is consistent with observations (Christiansen et al., 2000; Kastler and Wiberg, 1996). For small water depths (h<0.5 m), the maximum bed shear stress by tidal currents is set equal to τ_{cr}=1 Pa in order to filter out unrealistic erosion. Bed shear stresses and resulting erosion are calculated at multiple phases of the tidal cycle and integrated to incorporate the effect of intratidal velocity variability on sediment resuspension.

Ponding dynamics include pond formation by random seeding and impoundment, pond lateral expansion and deepening, and pond merging (Mariotti, 2020; Mariotti et al., 2020). Wind waves are calculated based on fetch, water depth, and wind speed (Young and Verhagen, 1996). Waves contribute to both bed sediment resuspension and marsh edge erosion. The latter is directly proportional to the wave power at the edge and implemented through a probabilistic approach (Mariotti and Canestrelli, 2017), assuming a proportionality coefficient of 0.2 m/y/W/m and a fixed fraction of oxidized material equal to 25%. Bed shear stress by waves is set equal to zero in the vegetated marsh.

2.2 Rationale for simulating stream meandering in tidal marshes

Compared to rivers, meandering in tidal streams might be perhaps treated more simply. Sediments are typically fine and cohesive and are mostly transported in suspension (Finotello et al., 2019a), such that the cross-stream bedload is not as important as it is for rivers. Hence, we argue that the main feature that needs to be reproduced is the lateral shift in flow momentum, as opposed to the entire cross-stream secondary circulation. We suggest a middle ground approach to recreate this effect by developing a simplified model based on the curvature of the flow rather than of the banks, which bears similarities to Nicholas's (2013) model for meandering rivers.

A modification of the base tidal flow field is then needed to induce two basic mechanisms: erosion at the outer concave bank (i.e., bank pull) and accretion at the inner convex bank (i.e., bar push) (Eke et al., 2014; van de Lageweg et al., 2014). Both mechanisms are critical, especially in tidal channels where banks do not necessarily move parallel to each other as a result of potential mutually-evasive paths followed by the ebb and flood flows (Ahnert, 1960). Eroding the outer

bank is needed to move the meander, whereas accreting the point bar at the inner bank is necessary to maintain the channel width in dynamic equilibrium and perpetuate channel meandering.

Special emphasis is given to formulating the model in a manner that enables its execution at coarse spatial resolutions, that is, for channels that have a width of just a few computational cells. Because channel width varies continuously, any marsh model would necessarily include channels that are one cell wide (unless spatial resolutions smaller than the smallest possible channels, on the order of 1 m, are used). When using coarse resolution (5-10 m), a large fraction of channels could still be only a few cells wide. Hence, it is important that the meandering model also works in this case.

2.3 Hydrodynamic model for curved flows

The curvature-driven modification should theoerically differ between ebb and flood (Finotello et al., 2020c). However, given that the model computes the same flow field for both ebb and flood ($\boldsymbol{U}$) (Eqs. 1,2), any difference in curved flow between ebb and flood is likely a second order effect compared to the assumptions already present in the model. Hence, to retain an appropriate level of complexity, we propose an empirical modification to the main flow field that is identical for both ebb and flood.

The first step is to account for the curvature effect is to identify the active flow region (Nicholas, 2013). For simplicity, we assume that the active flow region coincides with the unvegetated cells, although a distinction could also be made based on water depth and flow velocity. All other cells are considered hydrodynamically inactive. Inactive cells adjacent to active cells are considered bank cells. In practice, the flow domain coincides with the area lying below the lower limit for vegetation growth, which includes both the main channels and the mudflats.

The second step is to calculate, within the active flow region, the flow curvature strength (Φ):

$$\Phi = \left[\nabla x \widehat{\boldsymbol{U}}\right] |\boldsymbol{U}| h \tag{3}$$

where $\widehat{\boldsymbol{U}}$ is the velocity versor equal to $\boldsymbol{U}/|\boldsymbol{U}|$. The curvature is spatially smoothed along the cross-flow direction (i.e., perpendicular to the vector $\boldsymbol{U}$) within the active flow domain, with the purpose of creating a relatively uniform curvature field across the channel. The rationale of this step is that the cross-stream flow (responsible for carrying flow momentum outward) is produced as the result of a force balance within the whole channel cross-section (Solari et al., 2002). In addition, this smoothing tends to remove the curvature in channels that are not bounded by banks (i.e., mudflat channels). Notably, the curvature is not averaged in the along-stream direction to avoid the suppression of short wavelength instabilities that are the likely culprits of meander development (Seminara, 2006).

The third step is to use the flow curvature strength as a proxy for the modification of the flow field. Qualitatively, curvature tends to shift water flows from the inner to the outer meander bank. This effect is simulated by the parameter f:

$$f = min\left(1, \widehat{\boldsymbol{U}} \ [I + \nabla \cdot \boldsymbol{T}]^{-1}\right) \tag{4}$$

where $\boldsymbol{T} = a\Phi^b \widehat{\boldsymbol{U}}^{\perp}$ is a vector perpendicular to the main velocity $\boldsymbol{U}$, a and b are calibration parameters, and I is the identity matrix. The parameter f can be thought of as the velocity versor ($\widehat{\boldsymbol{U}}$) being advected laterally by a fictitious flow ($\boldsymbol{T}$) proportional to the flow curvature strength. In the absence of such lateral advection, the parameter f is equal to the unit everywhere. When the flow is in a divergent zone of the lateral advection $\boldsymbol{T}$ (e.g., the meander inner bank), f is smaller than one, whereas when the flow is in a convergent zone (e.g., the meander outer bank), the parameter is larger than one (Fig. 2). The a and b parameters are empirical calibration factors that cannot be derived from first principle. We found that a value of b smaller than one (e.g., equal to 0.5) provided a realistic flow field. The parameter a is set equal to 250.

The final step is to recalculate the velocity within the whole domain (Eqs. 1,2) by introducing f in the momentum equation:

$$\boldsymbol{U} \propto f \frac{h^{4/3}}{n^2} \nabla \eta \tag{5}$$

Preliminary tests indicated that, for complex geometry such as the intersection of channels, positive values of f occurred at unrealistic locations. On the other hand, negative values of f always occurred in the interior of bends. Furthermore, positive values of f (at bend outer edges) were highly sensitive to grid resolution, whereas negative values of f (at bend inner edges) were not. We found that the flow slowdown at the inner part of the bend (where f <1) sufficed to create a realistic flow over the whole domain. This is because velocity reduction at the inner bend automatically enhances velocities at the outer bank, given that Eq. 5 recalculates the flow in the whole domain. As such, values of f greater than one are set equal to one.

2.4 Curvature-induced outer bank erosion (bank pull)

The model includes two distinct mechanisms for bank erosion driven by sinuous flows. The first mechanism originates from a modification of the bank erosion process that is already present in the model, even without curvature correction. Flow is deflected to the outer banks, which increases bed scour in the proximity of the bank. This renders the bank steeper and consequently enhances elevation diffusion by soil creep (Mariotti et al., 2016, 2019).

The second mechanism entails bank erosion solely caused by the impact of curved flow on the bank, without any influence from the bed slope. Conceptually, this mechanism involves an active stripping of sediment from the bank, rather than a passive mass-wasting process. The rate of lateral bank erosion is set proportional to the flow curvature strength (Φ) at the outer bank:

$$E = k\Phi \tag{6}$$

This conceptualization is similar to previous centerline migration models used for meandering rivers (e.g., Bogoni et al., 2017; Frascati and Lanzoni, 2009; Seminara et al., 2001; Zolezzi and Seminara, 2001) and tidal creeks (e.g., Gong et al., 2018; Kleinhans et al., 2009), where bank erosion is linked to the near-bank excess velocity, the latter being however driven by the curvature of the channel axis rather than the flow. The coefficient of proportionality k is considered to be dependent on the soil strength and, more broadly, on the whole suite of hydro-mechanical processes that contribute to bank erosion. At this stage, however, k cannot be quantitatively linked to soil properties and is thus treated as an empirical parameter. Since banks are identified as vegetated cells adjacent to a non-vegetated cell (see Section 2.3), bank erosion

due to curved flows (Eq. 6) only occurs along salt-marsh channels where banks are vegetated. In theory, this mechanism could also be implemented in non-vegetated banks, which would, however, require defining the flow domain and the banks based on characteristics other than vegetation (e.g., a velocity threshold).

Operationally, lateral erosion predicted by Eq. 6 is often implemented through a reservoir method: partial erosion of a cell is stored until it reaches the size of a cell, at which point the entire cell is eroded by reducing its elevation (Nicholas, 2013). Here the lateral erosion is implemented with a probabilistic algorithm akin to that used to simulate wave-induced edge erosion (Mariotti and Canestrelli, 2017). This does not imply that bank erosion is a stochastic process but rather serves as a numerical approach to simulate lateral erosion in a domain represented by fixed cell locations and elevations. Once a cell has been eroded, a given portion of the material (25% in this case) is assumed to be removed through oxidation, while the remaining portion is redistributed among the neighboring cells.

2.5 Curvature-induced inner bank deposition (bar push)

Inner bend deposition is automatically reproduced in the model. Indeed, the curvature-induced modification of the basic flow field (Eq. 5) not only increases flow velocity at meander outer banks, but also reduces it at inner banks, thus promoting sediment deposition. This latter process does not require any ad hoc formulation, as it rather emerges from the sediment transport mechanism already present in the model.

The model also automatically includes a topographic steering effect (Lancaster and Bras, 2002). Indeed, the first-order flow already tends to allocate more flow where channels are deeper. Thus, if the scouring tends to occur toward the outer bank and deepens that part of the channel, more flow would be conveyed through that section by the first-order flow model. Then, the deposition in the inner bank increases the flow on the outer bank, which in turn increases the outside bank erosion through both mechanisms.

2.6 Representative numerical simulations

Model tests were performed considering an idealized tidal channel with a sinusoidal planform (amplitude of 150 m and a wavelength of either 400 or 800 m), a constant width of 40 m, and a constant depth of 3 m (Fig. 2). For simplicity, the tidal range was imposed equal to zero, and a constant tidal prism was imposed at the landward end so that the discharge was constant along the channel.

We also performed some idealized simulations inspired by two natural salt marshes (Fig. 1): Barnstable (Massachusetts, USA) and Bishops Head (Maryland, USA). The water level and wind inputs for each site are calculated as in Mariotti and Zapp (2022). Briefly, this accounts for the temporal variability in tidal range and sea level anomalies. Barnstable has a 10^{th} and 90^{th} tidal range of 2.21 and 3.63 m, a 10^{th} and 90^{th} sea level anomaly of -0.14 m and 0.13 m, and an upper limit for vegetation growth equal to 2.16 m above mean sea level. Bishops Head has a 10^{th} and 90^{th} tidal range of 0.41 and 0.67 m, a 10^{th} and 90^{th} sea level anomaly of -0.19 m and 0.19 m, and an upper limit for vegetation growth equal to 0.7 m above mean sea level. Both marshes have a semidiurnal tide, with a period of 12.5 hours. In both cases, we consider a marsh that is 2 km wide and 3 km long, with an additional 1 km long mudflat in front of it and an additional fetch of 1 km (Fig. 1). For the Barnstable case, we considered a characteristic suspended sediment concentration of 20 mg/L and a rate of relative sea level rise of 2.5 mm/yr, whereas for Bishops Head we

considered a characteristic suspended sediment concentration of 40 mg/L and a rate of relative sea level rise of 3.5 mm/yr, in agreement with field measurements (Wasson et al., 2019).

The reference simulation for both Barnstable and Bishops Head analogs used a grid resolution of 10 m, the flow correction to account for the effect of curvature (Eqs. 4,5), and a bank erosion coefficient k=0.2. Five additional simulations were conducted to test the model sensitivity by varying the grid resolution (to 5 m and 20 m, respectively), the value of the bank erosion coefficient (assuming k equal to 0 and 0.5), and by deactivating the flow correction based on curvature. A fixed computation timestep dt=0.5 years was used in all the simulations, with a total duration being equal to 3000 years. The standard simulations (with a grid resolution dx=10 m) took about 2 hours on a 3.2 GHz single-core processor.

The results of numerical simulations were analyzed to quantify the morphometric characteristics and planform dynamics of numerically-modeled meandering tidal channels. Details of this procedure are described in the Supplementary Information.

3 Results

3.1 Model Performance and Sensitivity

Simulations performed on individual meandering channels with constant depth demonstrate how the model provides a realistic curvature-induced modification of the flow (Fig. 2). Without such modification, the highest velocities are consistently found at inner convex banks, as expected by the balance between pressure gradient and bed friction. In contrast, threads of maximum velocity are shifted toward outer concave banks when the curvature-induced flow modification is included. Curvature-adjusted velocities are modified by up to 0.1 m/s compared to the base flow field (Fig. 2), which is generally on the order of 0.3 m/s. As expected, the flow modification is progressively stronger as the curvature increases (Fig. 2). Furthermore, the results suggest that the flow fields are similar regardless of the grid resolution, although higher resolutions yield more detailed results (Fig. 3).

The application of flow correction based on curvature yields satisfactory outcomes even when considering complex meandering networks rather than individual sinuous channels, indicating the model's suitability for use in such hydro-morphodynamically complex environments (Fig. 2). Importantly, the modified flow does not necessarily produce the highest velocity at the outer bank. Rather, flow maximum velocities can be found within the channel, typically aligned with the thalweg, especially in wide channels (Fig. 2).

The morphodynamic effect of curvature-induced flow modification on the network structure is readily visible when comparing it to cases where the correction is not implemented (Fig. 4). Without flow modification, channels are straight to mildy curved, consistent with previous simulations performed using the same numerical model (Mariotti, 2018, 2020) or other models that do not consider curvature-driven flow modifications (e.g., Belliard et al., 2015; Gourgue et al., 2022; Kirwan and Murray, 2007). In contrast, with the inclusion of flow-curvature correction, channels become highly sinuous, and closely resemble those observed at the reference sites (Fig. 1).

According to the model, the marsh platform in Bishops Head takes a few hundred years to establish, whereas the marsh platform in Barnstable takes about 1000 years, likely because of the lower sediment supply (Fig. 5). In both cases, the model predicts that the channels have a low

sinuosity when they initially form on the marsh platform, and that the sinuosity increases over the course of about 1000 years before stabilizing even though the channels keep migrating.

In addition to curvature-driven flow modifications, bank erodibility also plays a critical role in driving marsh morphodynamic evolution (Fig. 6). Interestingly, channels can become highly sinuous even without including lateral bank erosion (i.e., k=0). This is because channel banks can retreat and modify through bank creep alone. However, in this case, the lateral mobility of the channels is considerably reduced compared to scenarios where bank erodibility is considered. Overall, increasing the bank erodibility coefficient results in accelerated rates of channel meandering, regardless of channel size and environmental conditions (Fig. 6).

3.2 Quantitative analysis of meander morphology and dynamics

The model reproduces not only lateral channel migration – with the progressive erosion of concave outer banks and the formation of point bars on convex inner banks – but also realistic meander planform shape and cross-sectional morphology (Fig. 7). A comparison with existing data (Finotello et al., 2018, 2020a) highlights similar scaling of meander wavelengths, amplitudes, and radii of curvature as a function of meander width for both field and numerically modeled meanders (Fig. 7). Close similarity to field data is also observed in terms of meander width-to-depth ratios and cross-sectional shape. Notably, similar channel metrics are obtained when considering different spatial resolutions (Fig. 7,8).

Meander cross-sections are generally asymmetric and deeper toward the outer bank, which is often the case in fluvial and tidal channels alike (Fig. 9). Nonetheless, the channel thalweg is at times located closer to the inner bend (Fig. 9), which aligns with field observations (Fig. 10). Noticeably, both modeling results and the field observations indicate that this condition is typically associated with meanders exhibiting cuspate inner banks (Fig. 9,10), which are widely recognized as a diagnostic feature of tidal influence (Finotello et al., 2020c; Hughes, 2012; Woodroffe et al., 1989) (Fig. S2).

The reference simulations produce migration rates M_R= 0.039±0.14 m/yr for Barnstable and M_R=0.058±0.18 m/yr for Bishops Heads (Fig. 8). For comparison, the migration rates at those sites, estimated through aerial images considering the apex migration of about 30 meanders in the last 40 years, are on the order of 0.01-0.1 m/yr. Furthermore, width-adjusted rates of lateral meander migration (M_R^*=M_R/W) are equal to 0.13±0.54 % yr^{-1} at Barnstable and 0.23±0.77 % yr^{-1} at Bishops Head (Fig. 8), which broadly aligns with M_R^* observed in other tidal settings worldwide (Finotello et al., 2018; Gabet, 1998; Garofalo, 1980; Jarriel et al., 2021). Model results show that migration rates increase with increasing bank erosion coefficient (k). Numerical simulations carried out without curvature-flow correction exhibit the lowest migration rates, while the highest rates are observed when factoring in curvature correction and assuming a bank erodibility coefficient k=0.5 (Fig. 6). Different grid resolutions result in remarkably similar migration rates (Fig. 8).

4 Discussion

4.1 Model Performance and Comparison to Field Sites

The proposed model reproduces the ecomorphodynamic evolution of tidal marshes dissected by complex, branching, and meandering networks of tidal channels. Specifically, the model replicates meander cutoff (which is driven by intra-channel interactions) and channel

piracies (which is driven by inter-channel interactions), both of which are observed in real marshes (Fig. S4).

Unlike classic centerline migration models for meandering rivers – for which banks invariably move parallel to each other – our model allows channel banks to evolve independently. As a consequence, our model replicates the characteristic funneling of tidal channels, resulting from the progressive landward reduction of the tidal prism (Finotello et al., 2020a; Lanzoni and D'Alpaos, 2015). The model also recreates non-trivial meandering morphologies, such as meander bends characterized by cuspate inner banks (Fig. Fig. ,S2). Although these morphologies have traditionally been associated with mutually evasive paths followed by the ebb and flood flows (Ahnert, 1960; Dalrymple et al., 2012; Hughes, 2012), our model does not differentiate between ebb and flood. Therefore, the emergence of cuspate meanders from our numerical simulations suggests that the formation of cuspate bends may not necessarily be related to the above-described mechanism.

The gradual increase in channel sinuosity over time (Fig. 5) supports the hypothesis that mature marshes feature more extensive and sinuous tidal channels compared to juvenile marshes (Allen, 2000; Pethick, 1969), which is also supported by field examples. For example, the Barnstable marsh, which formed ca. 4000 years ago (Redfield, 1972), hosts a highly sinuous channel network (Fig. 1). In contrast, the Saeftinghe marsh (Western Scheldt Estuary, The Netherlands), which has a similar tidal range (about 4 m) but was only formed in the last 300 years, features lower channel sinuosities (Jongepier et al., 2015). On the other hand, previous studies showed that sinuosity might also be inherited from pre-existing sinuous mudflat channels that are progressively colonized by halophytic vegetation as marshes expand laterally (Belliard et al., 2015; Pestrong, 1972; Schwarz et al., 2014). Hence, we propose that elevated channel sinuosity does not always indicate marsh maturity, whereas the presence of meander cutoffs and channel piracies (Figs. S2,S3,S4) might serve as more reliable indicators.

4.2 Curvature-driven Meander Dynamics

Altough many factors have been proposed to control meander migration, previous studies emphasized the prominent role of curvature in determining not only migration rates but also the evolution of meander patterns in both tidal and fluvial landscapes (Fagherazzi et al., 2004; Finotello et al., 2018, 2022; Hooke, 2013; Lagasse et al., 2004; Sylvester et al., 2019). It is generally accepted that migration rates increase nonlinearly with curvature and tend to saturate when the radius of curvature becomes larger than 2-4 times the channel width (i.e., for width-adjusted radii of curvature $R^*=R/W>2$-4; Finotello et al., 2019; Hickin and Nanson, 1975; Hooke, 2013). These nonlinearities between migration and curvature are believed to arise from two contrasting effects. On the one hand, stronger channel curvature enhances both the secondary flow and the phase lag between curvature and near-bank velocity (Crosato, 2009; Lanzoni and Seminara, 2006; Parker et al., 1983; Seminara et al., 2001), resulting in more pronounced outer-bank erosion and migration. On the other hand, in sharp bends, the increase in curvature-induced effects is limited by the growth of hydrodynamic nonlinearities, such as saturation of secondary flow, enhanced secondary outer-bank flow cells, and flow separation at the outer bank (Blanckaert, 2011; Finotello et al., 2020c; Hooke, 2013), all of which contribute to slowing down bank erosion as curvature increases.

The relationships between modeled width-adjusted migration rates (M_R^*) and channel curvature (expressed through $R^*= R/W$) show positive correlations that tend to saturate for

increasing values of R^* (Fig. 8), in accordance with empirical observations. Since the model does not directly account for flow nonlinearities described above, other mechanisms are likely to explain the saturation of M_R^* at large curvature predicted by the model. First, curvature strength (Φ) affects the basic flow field in a nonlinear fashion, with curvature-induced flow modification being proportional to $\Phi^{0.5}$ (see Eq. 4). Second, some of the sediment eroded from the banks deposits in close proximity to the bank itself (see section 2.4), acting as a sheltering barrier and reducing the pace at which the bank retreats laterally (e.g., Eke et al., 2014; Motta et al., 2014; Posner and Duan, 2012). Indeed, field observations show that collapsed bank soil in salt marsh creeks could persist for several years (Fagherazzi et al., 2004), contributing to the channel erosion paradox (Gabet, 1998) whereby marsh creeks are likely to migrate laterally at a quite slow rate despite the widespread occurrence of collapsed bank blocks. Third, migration of the channel entails not only bank erosion but also channel thalweg migration, which occurs through bed erosion. Given that this process is not controlled by the flow curvature, it tends to slow down the overall migration for large flow curvatures.

Variability in bank erodibility is thought to explain the large scatter present in the curvature-migration relationship (Hooke, 2013; Nanson and Hickin, 1986; Schwendel et al., 2015). Despite the model having a spatially constant bank erodibility, however, there remains a considerable scatter between width-adjusted migration rate and channel curvature (Fig. 8). This is explained by considering that the channel curvature is only a proxy for the process driving channel migration, the real cause being the curved flow. For a given channel width and curvature, the flow can be different depending on the channel morphology (i.e., the depth and the position of the thalweg) and on the tidal prism passing through the cross section. Indeed, because of the frequent reorganization of the tidal network, a channel cross section might suddenly experience an increase or decrease in tidal prism, and hence change its migration rate.

Grid resolution can also alter the curvature-migration relationship by both affecting the numerical computation of curvature (Crosato, 2007) and setting the lower bound for migration rates that can be detected. Our analyses revealed that numerical simulations conducted with a grid resolution of dx=20 m yield poor correlations between M_R^* and R^*(especially for the Bishops Head case), suggesting that there exists a critical dx threshold beyond which the model struggles to accurately compute curvature and replicate its morphodynamic effects. The upcoming section provides a comprehensive discussion of the implications of grid resolution on modeled channel morphology and dynamics.

4.3 Effects of Computational Grid Resolution

The introduction of curvature-based flow modification leads to an increase in velocity near the outer bank and a decrease in velocity near the inner bank (Fig. 2). Consequently, this flow modification is not present in channels that are only one cell wide, where f=1 by definition (see Eq. 5). As a result, if the model creates channels that are one cell wide, these channels experience virtually no curvature-induced migration (except where they form 90 degree angles).

This limitation highlights the importance of selecting an appropriate grid resolution for numerical simulations. In the case of Barnstable, where most channels are wider than 10 m, resolutions $dx \leq$10 m are suitable for accurately representing the overall channel network structure (Fig. 11). With a resolution dx=20 m, in contrast, small channels become only one cell wide and thus do not exhibit significant migration (Fig. 11). Nevertheless, the channels in the main network branches are still replicated reasonably well. For the Bishops Head case, which features narrower

channels than Barnstable due to a smaller tidal range, a spatial resolution dx=20 m fails to reproduce most of the channels. Because the largest channels at Bishops Head are approximately 20 m wide, even the channels in the main network branches experience minimal migration and, as a result, exhibit poor sinuosity (Fig. 11).

To verify that the lack of migration in the Bishops Head case is due to reduced channel width rather than other factors (e.g., tidal range) or model shortcomings, an additional simulation was performed using a 10 km long domain, and replicated twice using a resolution dx=10 m and dx=20 m, respectively (Fig. 12). This extended domain increased the tidal prism in the seaward portion of the marsh, allowing for the formation of wider channels (Fig. 12). Even with dx=20 m, the model successfully replicated channel migration in the most seaward 3 km of the marsh, where channels were approximately 100 m wide. Yet, in the more landward regions, tidal channels remained narrower than 20 m and did not exhibit significant migration (Fig. 12), thus confirming our initial hypothesis.

4.4 Model Limitations and Future Developments

Modification of hydrodynamics in the model is currently implemented using an empirical approach. Future research could explore the possibility of deriving a simplified flow correction from a theoretical perspective in order to provide a robust and physically grounded understanding of the relationship between curvature and flow dynamics. This would contribute to enhancing the accuracy and reliability of the model in simulating meander migration processes.

The model utilizes a base flow field that does not account for tidal asymmetries. However, asymmetries in tidal flow velocities critically affect meander planform evolution by governing net in-channel sediment transport (Dronkers, 1986; Finotello et al., 2019a; Tambroni et al., 2017). Specifically, tidal meanders develop distinct depositional patterns based on the dominant flow direction, with flood-dominated flows leading to the formation of point bars upstream of bend apexes, and vice versa for ebb-dominated flows (Ghinassi et al., 2018; Tambroni et al., 2017). Although the model is capable of reproducing strongly skewed meander bends characterized by an asymmetry index ($\mathcal{A}$) significantly different from zero, the probability distributions of $\mathcal{A}$ for numerically modelled bends differ from the field data (Fig. S1). This is however a limitation of marginal importance. While local variations in tidal asymmetries can impact meander planform over relatively short timescales (i.e., decades), the overall evolution of the network structure on timescales ranging from centuries to millennia is more prominently influenced by inter and intra-channel dynamics (Fig. S3). This is because meander cutoffs and channel piracies can lead to significant reconfigurations of the network structure and related hydrological connectivity, and our model serves as a computationally efficient tool to replicate such dynamics.

Asymmetries in tidal flows can also lead to mutually evasive paths of ebb and flood currents, resulting in segregated ebb and flood channels separated by mid-channel bars (e.g., Leuven and Kleinhans, 2019; Robinson, 1960; Shimozono et al., 2019) (Fig. 10. These hydrodynamic nonlinearities, together with flow separation in sharp bends (Finotello et al., 2020c; Leeder and Bridges, 1975), are currently not accounted for. As a consequence, the model may generate narrower channels near the marsh seaward margin, which deviate from the channel characteristics observed in field studies (e.g., Barnstable; see Fig. 1). These limitations might also contribute to explaining the less pronounced saturation of migration rates beyond a critical R^* threshold compared to empirical field data, as well as the slightly shorter wavelengths of modeled meanders in comparison to those observed in nature (Fig. 7). It is worth noting that previous

models attempting to extend the theory of river bend instability to tidal meandering channels also encountered similar shortcomings (Solari et al., 2002).

Bank erodibility is currently calibrated to reproduce realistic rates of lateral migration. It would be interesting to explore in detail the relationship between the bank migration parameter (k) and soil properties such as bulk density, organic matter content, and vegetation root characteristics. A combination of modeling and field investigations can provide insights into the variation of bank erodibility among different marshes. Bank erodibility also changes with heterogeneous floodplain sedimentology, including fine-grained deposits sequestered in meander cutoffs and abandoned channels (Güneralp and Rhoads, 2011). Hence, future modeling efforts should aim at enabling the autogenic capacity of tidal channels to modify the surrounding tidal plains as they undergo lateral migration (e.g., Bogoni et al., 2017). In addition, future model development should consider the case of multiple sediment classes, e.g., both mud and sand. This would be particularly important to simulate sandy point-bar deposits.

5 Conclusions

We developed a novel numerical model to simulate channel meandering in tidal marshes. The key feature of the model is to compute the correction of the flow based on the curvature of the flow rather than the curvature of the bank. The model realistically recreates erosion of the outer bank (bank pull) and deposition in the inner bend (bar push). The model is highly numerically efficient and allows for simulating the ecomorphodynamic evolution of complex, branching and meandering networks of tidal channels over timescales ranging from centuries to millennia.

Our model represents a significant advancement in the study of tidal marshes as it enables the investigation of periodic reorganization in tidal channel networks, and hence marsh hydrological connectivity, at practically relevant spatial and temporal scales. This could be of particular importance for marsh conservation and restoration efforts.

Model applications to field and synthetic case studies will improve our understanding of the relationships between function and form in tidal channel networks. For instance, the model will facilitate the exploration of how lateral migration and meandering of tidal channels influence marsh ecology (e.g., vegetation), carbon and nutrient cycling, sedimentary dynamics, and stratigraphy.

Acknowledgments

This work was funded by the US Coastal Research Program through the US Army Engineer Research and Development Center, award #W912HZ2020029, to GM, as well as by the European Union – NextGenerationEU and by the University of Padua under the 2021 STARS Grants@Unipd programme (project "TiDyLLy – Tidal network dynamics as drivers for ecomorphodynamics of low-lying coastal regions" to AF.

The authors declare no conflicts of interest.

Open Research

The numerical model source code is freely available at:
csdms.colorado.edu/wiki/Model:MarshMorpho2D

References

Ahnert F. 1960. Estuarine Meanders in the Chesapeake Bay Area. Geographical Review **50** : 390. DOI: 10.2307/212282

Allen J. 2000. Morphodynamics of Holocene salt marshes: a review sketch from the Atlantic and Southern North Sea coasts of Europe. Quaternary Science Reviews **19** : 1155–1231. DOI: 10.1016/S0277-3791(99)00034-7

Belliard J-P, Toffolon M, Carniello L, D'Alpaos A. 2015. An ecogeomorphic model of tidal channel initiation and elaboration in progressive marsh accretional contexts. Journal of Geophysical Research: Earth Surface **120** : 1040–1064. DOI: 10.1002/2015JF003445

Belliard JP. 2014. Bio-physical controls on tidal network geomorphology, Univeristy of Trento, Trento, Italy

Blanckaert K. 2011. Hydrodynamic processes in sharp meander bends and their morphological implications. Journal of Geophysical Research: Earth Surface **116** : 1–22. DOI: 10.1029/2010JF001806

Bogoni M, Putti M, Lanzoni S. 2017. Modeling meander morphodynamics over self-formed heterogeneous floodplains. Water Resources Research **53** : 5137–5157. DOI: 10.1002/2017WR020726

Brivio L, Ghinassi M, D'Alpaos A, Finotello A, Fontana A, Roner M, Howes N. 2016. Aggradation and lateral migration shaping geometry of a tidal point bar: An example from salt marshes of the Northern Venice Lagoon (Italy). Sedimentary Geology **343** : 141–155. DOI: 10.1016/j.sedgeo.2016.08.005

Choi K, Jo JH. 2015. Morphodynamics of tidal channels in the open coast macrotidal flat, Southern Ganghwa Island in Gyeonggi Bay, west coast of Korea. Journal of Sedimentary Research **85** : 582–595. DOI: 10.2110/jsr.2015.44

Christiansen T, Wiberg PL, Milligan TG. 2000. Flow and sediment transport on a tidal salt marsh surface. Estuarine, Coastal and Shelf Science **50** : 315–331. DOI: 10.1006/ecss.2000.0548

Cleveringa J, Oost AP. 1999. The fractal geometry of tidal-channel systems in the Dutch Wadden Sea. Geologie en Mijnbouw/Netherlands Journal of Geosciences **78** : 21–30. DOI: 10.1023/A:1003779015372

Coco G, Zhou Z, van Maanen B, Olabarrieta M, Tinoco R, Townend I. 2013. Morphodynamics of tidal networks: Advances and challenges. Marine Geology **346** : 1–16. DOI: 10.1016/j.margeo.2013.08.005

Cosma M, Finotello A, Ielpi A, Ventra D, Oms O, D'Alpaos A, Ghinassi M. 2020. Piracy-controlled geometry of tide-dominated point bars: Combined evidence from ancient sedimentary successions and modern channel networks. Geomorphology **370** : 107402. DOI: 10.1016/j.geomorph.2020.107402

Cosma M, Ghinassi M, D'Alpaos A, Roner M, Finotello A, Tommasini L, Gatto R. 2019. Point-bar brink and channel thalweg trajectories depicting interaction between vertical and lateral shifts of microtidal channels in the Venice Lagoon (Italy). Geomorphology **342** : 37–50. DOI: 10.1016/j.geomorph.2019.06.009

Coulthard TJ, Van De Wiel MJ. 2012. Modelling river history and evolution. Philosophical Transactions of the Royal Society A: Mathematical, Physical and Engineering Sciences **370** : 2123–2142. DOI: 10.1098/rsta.2011.0597

Crosato A. 2007. Effects of smoothing and regridding in numerical meander migration models. Water Resources Research **43** : 1–10. DOI: 10.1029/2006WR005087

Crosato A. 2009. Physical explanations of variations in river meander migration rates from model comparison. Earth Surface Processes and Landforms **34** : 2078–2086. DOI: 10.1002/esp.1898

D'Alpaos A, Lanzoni S, Marani M, Fagherazzi S, Rinaldo A. 2005. Tidal network ontogeny: Channel initiation and early development. Journal of Geophysical Research: Earth Surface **110** : 1–14. DOI: 10.1029/2004JF000182

D'Alpaos A, Lanzoni S, Marani M, Rinaldo A. 2007. Landscape evolution in tidal embayments: Modeling the interplay of erosion, sedimentation, and vegetation dynamics. Journal of Geophysical Research: Earth Surface **112** : 1–17. DOI: 10.1029/2006JF000537

Dalrymple RW, Mackay DA, Ichaso AA, Choi KS. 2012. Processes, Morphodynamics, and Facies of Tide-Dominated Estuaries. In Principles of Tidal Sedimentology , Davis Jr. RA and Dalrymple RW (eds). Springer Science+Business Media: Dordrecht; 79–107.

Dronkers J. 1986. Tidal asymmetry and estuarine morphology. Netherlands Journal of Sea Research **20** : 117–131. DOI: 10.1016/0077-7579(86)90036-0

Duvall MS, Wiberg PL, Kirwan ML. 2019. Controls on Sediment Suspension, Flux, and Marsh Deposition near a Bay-Marsh Boundary. Estuaries and Coasts **42** : 403–424. DOI: 10.1007/s12237-018-0478-4

Eke E, Parker G, Shimizu Y. 2014. Numerical modeling of erosional and depositional bank processes in migrating river bends with self-formed width: Morphodynamics of bar push and bank pull. Journal of Geophysical Research: Earth Surface **119** : 1455–1483. DOI: 10.1002/2013JF003020

Elsey-Quirk T, Mariotti G, Valentine K, Raper K. 2019. Retreating marsh shoreline creates hotspots of high-marsh plant diversity. Scientific Reports **9** : 1–9. DOI: 10.1038/s41598-019-42119-8

Fagherazzi S, Bortoluzzi A, Dietrich WE, Adami A, Lanzoni S, Marani M, Rinaldo A. 1999. Tidal networks 1. Automatic network extraction and preliminary scaling features from digital terrain maps. Water Resources Research **35** : 3891–3904. DOI: 10.1029/1999WR900236

Fagherazzi S, Gabet EJ, Furbish DJ. 2004. The effect of bidirectional flow on tidal channel planforms. Earth Surface Processes and Landforms **29** : 295–309. DOI: 10.1002/esp.1016

Fagherazzi S, Sun T. 2004. A stochastic model for the formation of channel networks in tidal marshes. Geophysical Research Letters **31** : 1–4. DOI: 10.1029/2004GL020965

Finotello A, Canestrelli A, Carniello L, Ghinassi M, D'Alpaos A. 2019a. Tidal Flow Asymmetry and Discharge of Lateral Tributaries Drive the Evolution of a Microtidal Meander in the Venice Lagoon (Italy). Journal of Geophysical Research: Earth Surface **124** : 3043–3066. DOI: 10.1029/2019JF005193

Finotello A, Capperucci RM, Bartholomä A, D'Alpaos A, Ghinassi M. 2022. Morpho-sedimentary evolution of a microtidal meandering channel driven by 130 years of natural and anthropogenic modifications of the Venice Lagoon (Italy). Earth Surface Processes and Landforms **47** : 2580–2596. DOI: 10.1002/esp.5396

Finotello A, D'Alpaos A, Bogoni M, Ghinassi M, Lanzoni S. 2020a. Remotely-sensed planform morphologies reveal fluvial and tidal nature of meandering channels. Scientific Reports **10** : 1–13. DOI: 10.1038/s41598-019-56992-w

Finotello A, D'Alpaos A, Lazarus ED, Ghinassi M, Rinaldo A. 2020b. Meander cutoffs in tidal coastal landscapes : rare of everywhere ? 18018 pp.

Finotello A, D'Alpaos A, Lazarus ED, Lanzoni S. 2019b. High curvatures drive river meandering: COMMENT. Geology **47** : e485–e485. DOI: 10.1130/G46761C.1

Finotello A, Ghinassi M, Carniello L, Belluco E, Pivato M, Tommasini L, D'Alpaos A. 2020c. Three-Dimensional Flow Structures and Morphodynamic Evolution of Microtidal Meandering Channels. Water Resources Research **56** : e2020WR027822. DOI: 10.1029/2020WR027822

Finotello A, Lanzoni S, Ghinassi M, Marani M, Rinaldo A, D'Alpaos A. 2018. Field migration rates of tidal meanders recapitulate fluvial morphodynamics. Proceedings of the National Academy of Sciences of the United States of America **115** : 1463–1468. DOI: 10.1073/pnas.1711330115

Frascati A, Lanzoni S. 2009. Morphodynamic regime and long-term evolution of meandering rivers. Journal of Geophysical Research: Earth Surface **114** : 1–12. DOI: 10.1029/2008JF001101

Gabet EJ. 1998. Lateral Migration and Bank Erosion in a Saltmarsh Tidal Channel in San Francisco Bay, California. Estuaries **21** : 745. DOI: 10.2307/1353278

Gao C, Finotello A, D'Alpaos A, Ghinassi M, Carniello L, Pan Y, Chen D, Wang YP. 2022. Hydrodynamics of Meander Bends in Intertidal Mudflats: A Field Study From the Macrotidal Yangkou Coast, China. Water Resources Research **58** : 1–28. DOI: 10.1029/2022WR033234

Garofalo D. 1980. The Influence of Wetland Vegetation on Tidal Stream Channel Migration and Morphology. Estuaries **3** : 258. DOI: 10.2307/1352081

Gasparotto A, Darby SE, Leyland J, Carling PA. 2022. Water level fluctuations drive bank instability in a hypertidal estuary. Earth Surface Dynamics **2080** : 1–28.

Geng L, Gong Z, Zhou Z, Lanzoni S, D'Alpaos A. 2020. Assessing the relative contributions of the flood tide and the ebb tide to tidal channel network dynamics. Earth Surface Processes and Landforms **45** : 237–250. DOI: 10.1002/esp.4727

Ghinassi M et al. 2018. Morphodynamic evolution and stratal architecture of translating tidal point bars: Inferences from the northern Venice Lagoon (Italy). Sedimentology **65** : 1354–1377. DOI: 10.1111/sed.12425

Gong Z, Zhao K, Zhang C, Dai W, Coco G, Zhou Z. 2018. The role of bank collapse on tidal creek ontogeny: A novel process-based model for bank retreat. Geomorphology **311** : 13–26. DOI: 10.1016/j.geomorph.2018.03.016

Gourgue O, van Belzen J, Schwarz C, Vandenbruwaene W, Vanlede J, Belliard JP, Fagherazzi S, Bouma TJ, van de Koppel J, Temmerman S. 2022. Biogeomorphic modeling to assess the resilience of tidal-marsh restoration to sea level rise and sediment supply. Earth Surface Dynamics **10** : 531–553. DOI: 10.5194/esurf-10-531-2022

Güneralp I, Abad JD, Zolezzi G, Hooke J. 2012. Advances and challenges in meandering channels research. Geomorphology **163**–**164** : 1–9. DOI: 10.1016/j.geomorph.2012.04.011

Güneralp Í, Rhoads BL. 2011. Influence of floodplain erosional heterogeneity on planform complexity of meandering rivers. Geophysical Research Letters **38** : L14401. DOI: 10.1029/2011GL048134

Hickin EJ, Nanson GC. 1975. The Character of Channel Migration on the Beatton River, Northeast British Columbia, Canada. Geological Society of America Bulletin **86** : 487. DOI: 10.1130/0016-7606(1975)86<487:TCOCMO>2.0.CO;2

Hood WG. 2014. Differences in tidal channel network geometry between reference marshes and marshes restored by historical dike breaching. Ecological Engineering **71** : 563–573. DOI: 10.1016/j.ecoleng.2014.07.076

Hooke JM. 2013. River Meandering. In Treatise on Geomorphology , Wohl E and Schroder (eds). Elsevier: Washington; 260–288.

Hopkinson CS, Morris JT, Fagherazzi S, Wollheim WM, Raymond PA. 2018. Lateral Marsh Edge Erosion as a Source of Sediments for Vertical Marsh Accretion. Journal of Geophysical Research: Biogeosciences **123** : 2444–2465. DOI: 10.1029/2017JG004358

Howard AD, Knutson TR. 1984. Sufficient conditions for river meandering: A simulation approach. Water Resources Research **20** : 1659–1667. DOI: 10.1029/WR020i011p01659

Hughes ZJ. 2012. Tidal channels on tidal flats and marshes. In Principles of Tidal Sedimentology , Davis RA and Dalrymple RW (eds). Springer: Dordrecht; 269–300.

Ikeda S, Parker G, Sawai K. 1981. Bend theory of river meanders. Part 1. Linear development. Journal of Fluid Mechanics **112** : 363–377. DOI: 10.1017/S0022112081000451

Jarriel T, Swartz J, Passalacqua P. 2021. Global rates and patterns of channel migration in river deltas. Proceedings of the National Academy of Sciences of the United States of America **118** DOI: 10.1073/pnas.2103178118

Jongepier I, Wang C, Missiaen T, Soens T, Temmerman S. 2015. Intertidal landscape response time to dike breaching and stepwise re-embankment: A combined historical and geomorphological study. Geomorphology **236** : 64–78. DOI: 10.1016/j.geomorph.2015.02.012

Kalra TS, Ganju NK, Aretxabaleta AL, Carr JA, Defne Z, Moriarty JM. 2021. Modeling Marsh Dynamics Using a 3-D Coupled Wave-Flow-Sediment Model. Frontiers in Marine Science **8** DOI: 10.3389/fmars.2021.740921

Kastler JA, Wiberg PL. 1996. Sedimentation and Boundary Changes of Virginia Salt Marshes. Estuarine, Coastal and Shelf Science **42** : 683–700. DOI: https://doi.org/10.1006/ecss.1996.0044

Kearney WS, Fagherazzi S. 2016. Salt marsh vegetation promotes efficient tidal channel

networks. Nature Communications **7** : 1–7. DOI: 10.1038/ncomms12287

Kirwan ML, Murray AB. 2007. A coupled geomorphic and ecological model of tidal marsh evolution. Proceedings of the National Academy of Sciences of the United States of America **104** : 6118–6122. DOI: 10.1073/pnas.0700958104

Kleinhans MG, Van Scheltinga RT, Van Der Vegt M, Markies H. 2015. Turning the tide: Growth and dynamics of a tidal basin and inlet in experiments. Journal of Geophysical Research: Earth Surface **120** : 95–119. DOI: 10.1002/2014JF003127

Kleinhans MG, Schuurman F, Bakx W, Markies H. 2009. Meandering channel dynamics in highly cohesive sediment on an intertidal mud flat in the Westerschelde estuary, the Netherlands. Geomorphology **105** : 261–276. DOI: 10.1016/j.geomorph.2008.10.005

Konkol A, Schwenk J, Katifori E, Shaw JB. 2022. Interplay of River and Tidal Forcings Promotes Loops in Coastal Channel Networks. Geophysical Research Letters **49** DOI: 10.1029/2022gl098284

Lacy JR, Foster-Martinez MR, Allen RM, Ferner MC, Callaway JC. 2020. Seasonal Variation in Sediment Delivery Across the Bay-Marsh Interface of an Estuarine Salt Marsh. Journal of Geophysical Research: Oceans **125** : 1–21. DOI: 10.1029/2019JC015268

Lagasse PF, Zevenbergen L, Spitz W, Thorne CR. 2004. A Methodology for Predicting Channel Migration NCHRP Project No. 24-16 . Fort Collins, CO

van de Lageweg WI, van Dijk WM, Baar AW, Rutten J, Kleinhans MG. 2014. Bank pull or bar push: What drives scroll-bar formation in meandering rivers? Geology **42** : 319–322. DOI: 10.1130/G35192.1

Lancaster ST, Bras RL. 2002. A simple model of river meandering and its comparison to natural channels. Hydrological Processes **16** : 1–26. DOI: 10.1002/hyp.273

Lanzoni S, D'Alpaos A. 2015. On funneling of tidal channels. Journal of Geophysical Research: Earth Surface **120** : 433–452. DOI: 10.1002/2014JF003203

Lanzoni S, Seminara G. 2006. On the nature of meander instability. Journal of Geophysical Research: Earth Surface **111** : 1–14. DOI: 10.1029/2005JF000416

Leeder MR, Bridges PH. 1975. Flow separation in meander bends. Nature **253** : 338–339. DOI: 10.1038/253338a0

Leonardi N, Defne Z, Ganju NK, Fagherazzi S. 2016. Salt marsh erosion rates and boundary features in a shallow Bay. Journal of Geophysical Research: Earth Surface **121** : 1861–1875. DOI: 10.1002/2016JF003975

Leopold LB, Wolman MG. 1960. River meanders. Bulletin of the Geological Society of America **71** : 769–793. DOI: 10.1130/0016-7606(1960)71[769:RM]2.0.CO;2

Letzsch WS, Frey RW. 1980. Deposition and erosion in a Holocene salt marsh, Sapelo Island, Georgia. Journal of Sedimentary Petrology **50** : 529–542. DOI: 10.1306/212F7A45-2B24-11D7-8648000102C1865D

Leuven JRFW, Kleinhans MG. 2019. Incipient Tidal Bar and Sill Formation. Journal of Geophysical Research: Earth Surface **124** : 1762–1781. DOI: 10.1029/2018JF004953

Litwin RJ, Smoot JP, Pavich MJ, Oberg E, Steury B, Helwig B, Markewich HW, Santucci VL,

Sanders G. 2013. Rates and probable causes of freshwater tidal marsh failure, Potomac River estuary, Northern Virginia, USA. Wetlands **33** : 1037–1061. DOI: 10.1007/s13157-013-0461-6

Van Maanen B, Coco G, Bryan KR. 2013. Modelling the effects of tidal range and initial bathymetry on the morphological evolution of tidal embayments. Geomorphology **191** : 23–34. DOI: 10.1016/j.geomorph.2013.02.023

Marani M, Belluco E, D'Alpaos A, Defina A, Lanzoni S, Rinaldo A. 2003. On the drainage density of tidal networks. Water Resources Research **39** : 1–11. DOI: 10.1029/2001WR001051

Marani M, Lanzoni S, Zandolin D, Seminara G, Rinaldo A. 2002. Tidal meanders. Water Resources Research **38** : 7-1-7–14. DOI: 10.1029/2001wr000404

Mariotti G. 2018. Marsh channel morphological response to sea level rise and sediment supply. Estuarine, Coastal and Shelf Science **209** : 89–101. DOI: 10.1016/j.ecss.2018.05.016

Mariotti G. 2020. Beyond marsh drowning: The many faces of marsh loss (and gain). Advances in Water Resources **144** : 103710. DOI: 10.1016/j.advwatres.2020.103710

Mariotti G, Canestrelli A. 2017. Long-term morphodynamics of muddy backbarrier basins: Fill in or empty out? Water Resources Research **53** : 7029–7054. DOI: 10.1002/2017WR020461

Mariotti G, Kearney WS, Fagherazzi S. 2016. Soil creep in salt marshes. Geology **44** : 459–462. DOI: 10.1130/G37708.1

Mariotti G, Kearney WS, Fagherazzi S. 2019. Soil creep in a mesotidal salt marsh channel bank: Fast, seasonal, and water table mediated. Geomorphology **334** : 126–137. DOI: https://doi.org/10.1016/j.geomorph.2019.03.001

Mariotti G, Spivak AC, Luk SY, Ceccherini G, Tyrrell M, Gonneea ME. 2020. Modeling the spatial dynamics of marsh ponds in New England salt marshes. Geomorphology **365** : 107262. DOI: 10.1016/j.geomorph.2020.107262

Mariotti G, Zapp SM. 2022. A Framework to Simplify Astro-Meteorological Water Level and Wind Inputs for Modeling Coastal Marsh Ecomorphodynamics. Journal of Geophysical Research: Earth Surface **127** : 1–26. DOI: 10.1029/2022JF006665

Morris JT, Sundareshwar P V., Nietch CT, Kjerfve B, Cahoon DR. 2002. Responses of coastal wetlands to rising sea level. Ecology **83** : 2869–2877. DOI: 10.1890/0012-9658(2002)083[2869:ROCWTR]2.0.CO;2

Motta D, Langendoen EJ, Abad JD, García MH. 2014. Modification of meander migration by bank failures. Journal of Geophysical Research: Earth Surface **119** : 1026–1042. DOI: 10.1002/2013JF002952

Nanson GC, Hickin EJ. 1986. A statistical analysis of bank erosion and channel migration in western Canada. Geological Society of America Bulletin **97** : 497–504. DOI: 10.1130/0016-7606(1986)97<497:ASAOBE>2.0.CO;2

Nicholas AP. 2013. Modelling the continuum of river channel patterns. Earth Surface Processes and Landforms **38** : 1187–1196. DOI: 10.1002/esp.3431

Parker G, Diplas P, Akiyama J. 1983. Meander Bends of High Amplitude. Journal of Hydraulic

Engineering **109** : 1323–1337. DOI: 10.1061/(asce)0733-9429(1983)109:10(1323)

Parker G, Sawai K, Ikeda S. 1982. Bend theory of river meanders. Part 2. Nonlinear deformation of finite-amplitude bends. Journal of Fluid Mechanics **115** : 303–314. DOI: 10.1017/S0022112082000767

Pestrong R. 1972. Tidal-flat sedimentation at cooley landing, Southwest San Francisco bay. Sedimentary Geology **8** : 251–288. DOI: 10.1016/0037-0738(72)90044-9

Pethick JS. 1969. Drainage in salt marshes. In The Coastline of England and Wales (3rd edition) , Steers JR (ed). Cambridge University Press: Cambridge; 730–752.

Posner AJ, Duan JG. 2012. Simulating river meandering processes using stochastic bank erosion coefficient. Geomorphology **163**–**164** : 26–36. DOI: 10.1016/j.geomorph.2011.05.025

Redfield AC. 1972. Development of a New England Salt Marsh. Ecological Monographs **42** : 201–237. DOI: 10.2307/1942263

Rinaldo A, Fagherazzi S, Lanzoni S, Marani M, Dietrich WE. 1999a. Tidal networks 2. Watershed delineation and comparative network morphology. Water Resources Research **35** : 3905–3917. DOI: 10.1029/1999WR900237

Rinaldo A, Fagherazzi S, Lanzoni S, Marani M, Dietrich WE. 1999b. Tidal networks 3. Landscape-forming discharges and studies in empirical geomorphic relationships. Water Resources Research **35** : 3919–3929. DOI: 10.1029/1999WR900238

Rizzetto F, Tosi L. 2012. Rapid response of tidal channel networks to sea-level variations (Venice Lagoon, Italy). Global and Planetary Change **92**–**93** : 191–197. DOI: 10.1016/j.gloplacha.2012.05.022

Robinson AHW. 1960. Ebb-flood Channel Systems in Sandy Bays and Estuaries. Geography **45** : 183–199.

Schwarz C, Ye QH, Van Der Wal D, Zhang LQ, Bouma T, Ysebaert T, Herman PMJ. 2014. Impacts of salt marsh plants on tidal channel initiation and inheritance. Journal of Geophysical Research: Earth Surface **119** : 385–400. DOI: 10.1002/2013JF002900

Schwendel AC, Nicholas AP, Aalto RE, Sambrook Smith GH, Buckley S. 2015. Interaction between meander dynamics and floodplain heterogeneity in a large tropical sand-bed river: The Rio Beni, Bolivian Amazon. Earth Surface Processes and Landforms **40** : 2026–2040. DOI: 10.1002/esp.3777

Seminara G. 2006. Meanders. Journal of Fluid Mechanics **554** : 271–297. DOI: 10.1017/S0022112006008925

Seminara G, Zolezzi G, Tubino M, Zardi D. 2001. Downstream and upstream influence in river meandering. Part 2. Planimetric development. Journal of Fluid Mechanics **438** : 213–230. DOI: 10.1017/S0022112001004281

Shimozono T, Tajima Y, Akamatsu S, Matsuba Y, Kawasaki A. 2019. Large-Scale Channel Migration in the Sittang River Estuary. Scientific Reports **9** : 1–9. DOI: 10.1038/s41598-019-46300-x

Di Silvio G, Dall'Angelo C, Bonaldo D, Fasolato G. 2010. Long-term model of planimetric and bathymetric evolution of a tidal lagoon. Continental Shelf Research **30** : 894–903. DOI:

10.1016/j.csr.2009.09.010

Solari L, Seminara G, Lanzoni S, Marani M, Rinaldo A. 2002. Sand bars in tidal channels part 2. Tidal meanders. Journal of Fluid Mechanics **451** : 203–238. DOI: 10.1017/s0022112001006565

Stefanon L, Carniello L, D'Alpaos A, Rinaldo A. 2012. Signatures of sea level changes on tidal geomorphology: Experiments on network incision and retreat. Geophysical Research Letters **39** : 1–6. DOI: 10.1029/2012GL051953

Sylvester Z, Durkin P, Covault JA, Sharman GR. 2019. High curvatures drive river meandering. Geology **47** : e486–e486. DOI: 10.1130/G46838Y.1

Tambroni N, Luchi R, Seminara G. 2017. Can tide dominance be inferred from the point bar pattern of tidal meandering channels? Journal of Geophysical Research: Earth Surface **122** : 492–512. DOI: 10.1002/2016JF004139

Wasson K, Ganju NK, Defne Z, Endris C, Elsey-Quirk T, Thorne KM, Freeman CM, Guntenspergen G, Nowacki DJ, Raposa KB. 2019. Understanding tidal marsh trajectories: Evaluation of multiple indicators of marsh persistence. Environmental Research Letters **14** DOI: 10.1088/1748-9326/ab5a94

Wilson C, Goodbred S, Small C, Gilligan J, Sams S, Mallick B, Hale R. 2017. Widespread infilling of tidal channels and navigable waterways in the human-modified tidal deltaplain of southwest Bangladesh. Elementa **5** DOI: 10.1525/elementa.263

Woodroffe CD, Chappell J, Thom BG, Wallensky E. 1989. Depositional model of a macrotidal estuary and floodplain, South Alligator River, Northern Australia. Sedimentology **36** : 737–756. DOI: 10.1111/j.1365-3091.1989.tb01743.x

Xu F, Coco G, Zhou Z, Tao J, Zhang C. 2017. A numerical study of equilibrium states in tidal network morphodynamics. : 1593–1607. DOI: 10.1007/s10236-017-1101-0

Young IR, Verhagen LA. 1996. The growth of fetch limited waves in water of finite depth. Part 1. Total energy and peak frequency. Coastal Engineering **29** : 47–78. DOI: 10.1016/S0378-3839(96)00006-3

Zhao K, Coco G, Gong Z, Darby SE, Lanzoni S, Xu F, Zhang K, Townend I. 2022. A Review on Bank Retreat: Mechanisms, Observations, and Modeling. Reviews of Geophysics **60** : 1–51. DOI: 10.1029/2021rg000761

Zhou Z, Olabarrieta M, Stefanon L, D'Alpaos A, Carniello L, Coco G. 2014a. A comparative study of physical and numerical modeling of tidal network ontogeny. Journal of Geophysical Research: Earth Surface **119** : 892–912. DOI: 10.1002/2014JF003092

Zhou Z, Stefanon L, Olabarrieta M, D'alpaos A, Carniello L, Coco G. 2014b. Analysis of the drainage density of experimental and modelled tidal networks. Earth Surface Dynamics **2** : 105–116. DOI: 10.5194/esurf-2-105-2014

Zolezzi G, Seminara G. 2001. Downstream and upstream influence in river meandering. Part 1. General theory and application overdeepening. Journal of Fluid Mechanics **438** : 183–211. DOI: 10.1017/S002211200100427X

Figures

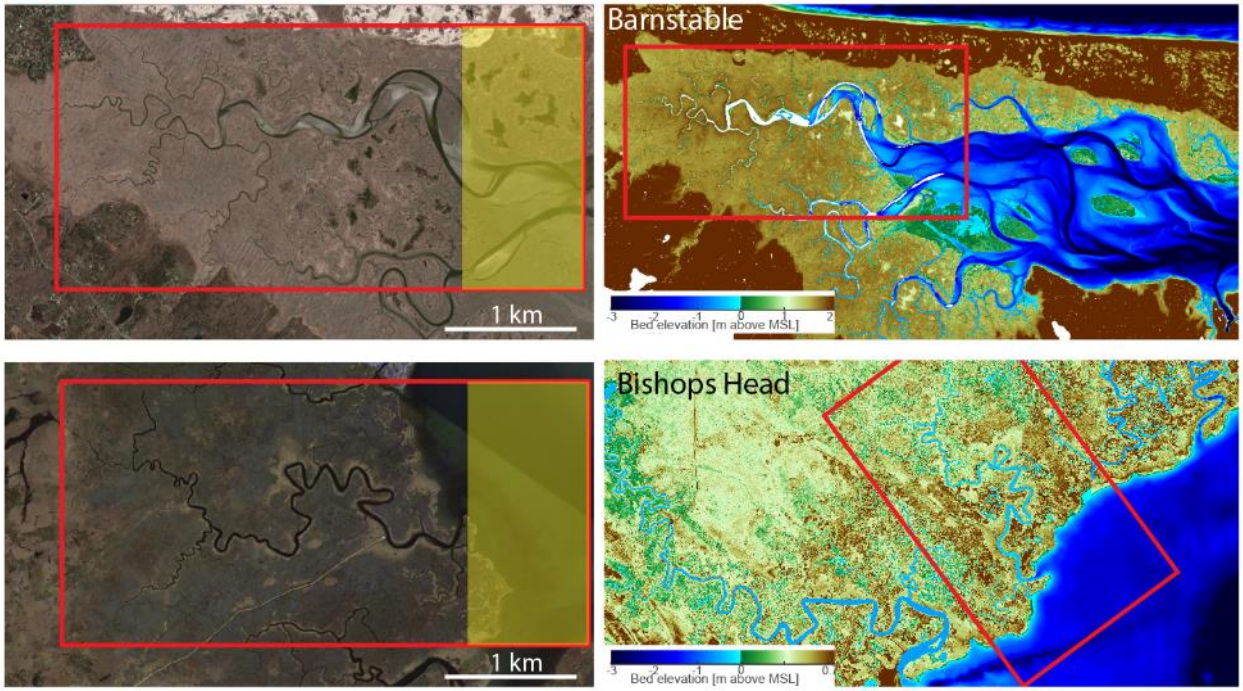

Figure 1. Aerial images and topobathymetric maps of salt marshes found in Barnstable (Massachusetts, USA) and Bishops Head (Maryland, USA). The red rectangles indicate the size of the computational domain used in numerical simulations, which also includes the adjacent mudflat highlighted in yellow. Note that channel depths in Bishops Head are underestimated as they are based on elevations of the water surface rather than of channel bed.

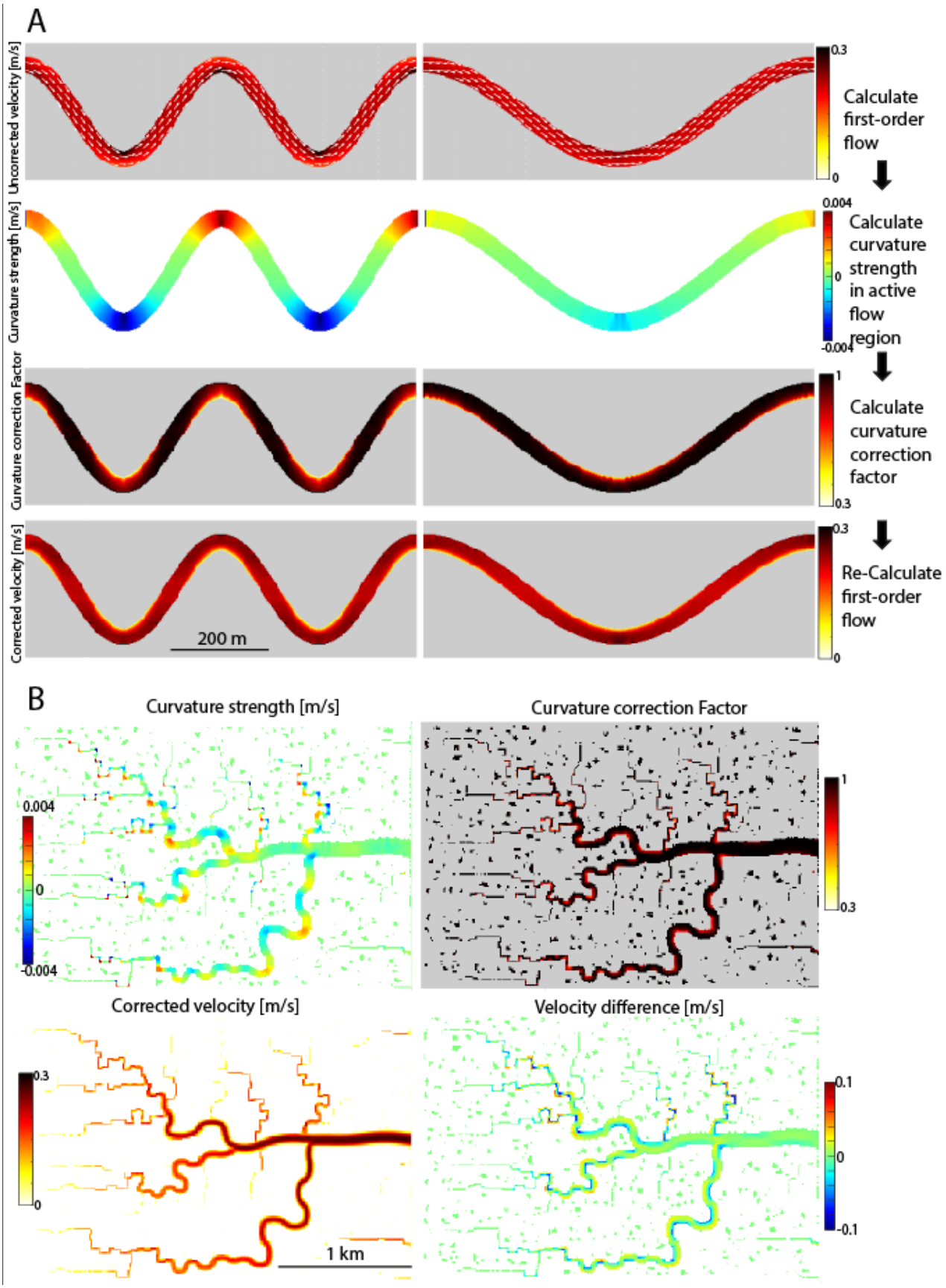
A
Uncorrected velocity [m/s]
0.3
0
Calculate first-order flow
Curvature strength [m/s]
0.004
0
-0.004
Calculate curvature strength in active flow region
Curvature correction Factor
1
0.3
Calculate curvature correction factor
Corrected velocity [m/s]
0.3
0
Re-Calculate first-order flow
200 m
B
Curvature strength [m/s]
0.004
0
-0.004
Curvature correction Factor
1
0.3
Corrected velocity [m/s]
0.3
0
1 km
Velocity difference [m/s]
0.1
0
-0.1

Figure 2. Example of the calculated flow field. A) Application of the model to a regular sinusoidal channel characterized by an amplitude of 150 m, a constant width of 40 m, a fixed depth of 3 m, and a wavelength of either 400 m (left column) or 800 m (right column). The resolution of the computational grid is equal to *dx*=2.5 m. Moving from top to bottom, each panel illustrates a different computational step to account for curvature-induced hydrodynamic adjustments, as indicated by the legend to the right. B) Application of the model in the case of a morphologically complex tidal channel network simulated by the model, similar to the one depicted in Fig. 4A, using a tidal range equal to 3 m.

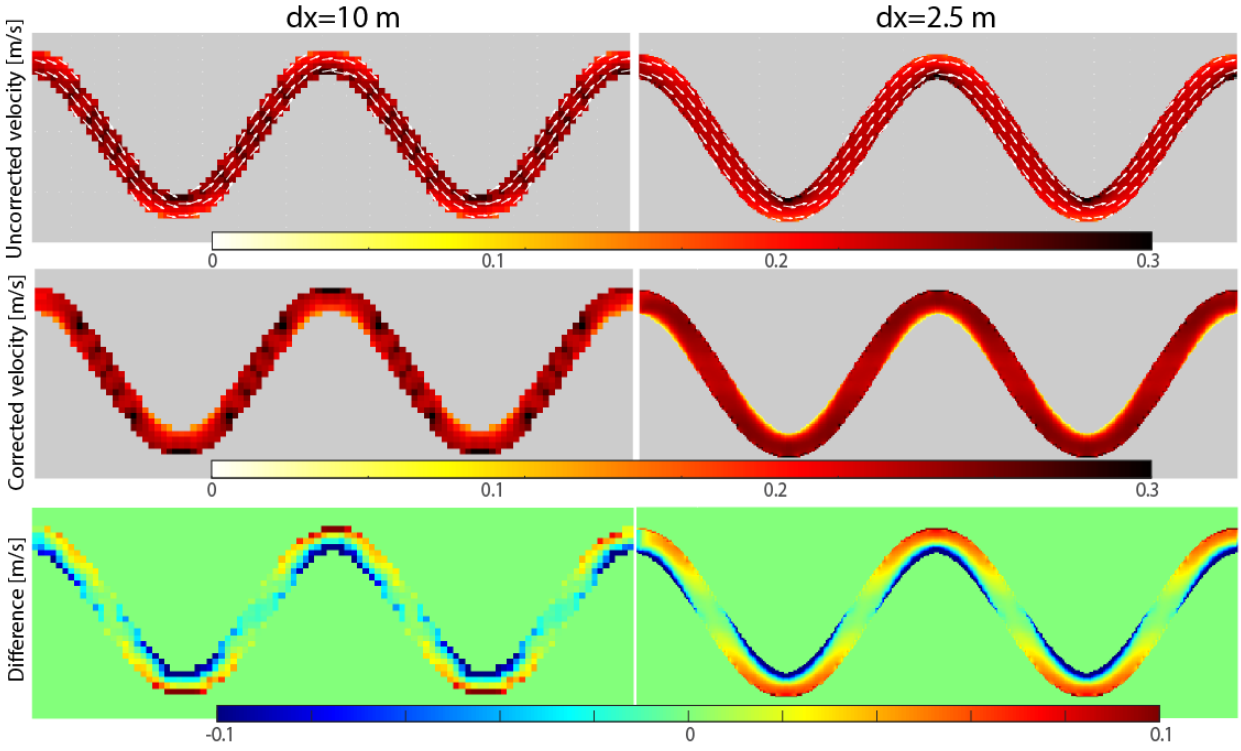

Figure 3: Comparison of the flow in a regular sinusoidal channel with and without curvature-driven flow modification. Results are reported for the same geometry and with two grid resolutions equal to *dx*=10 m and *dx*=2.5 m.

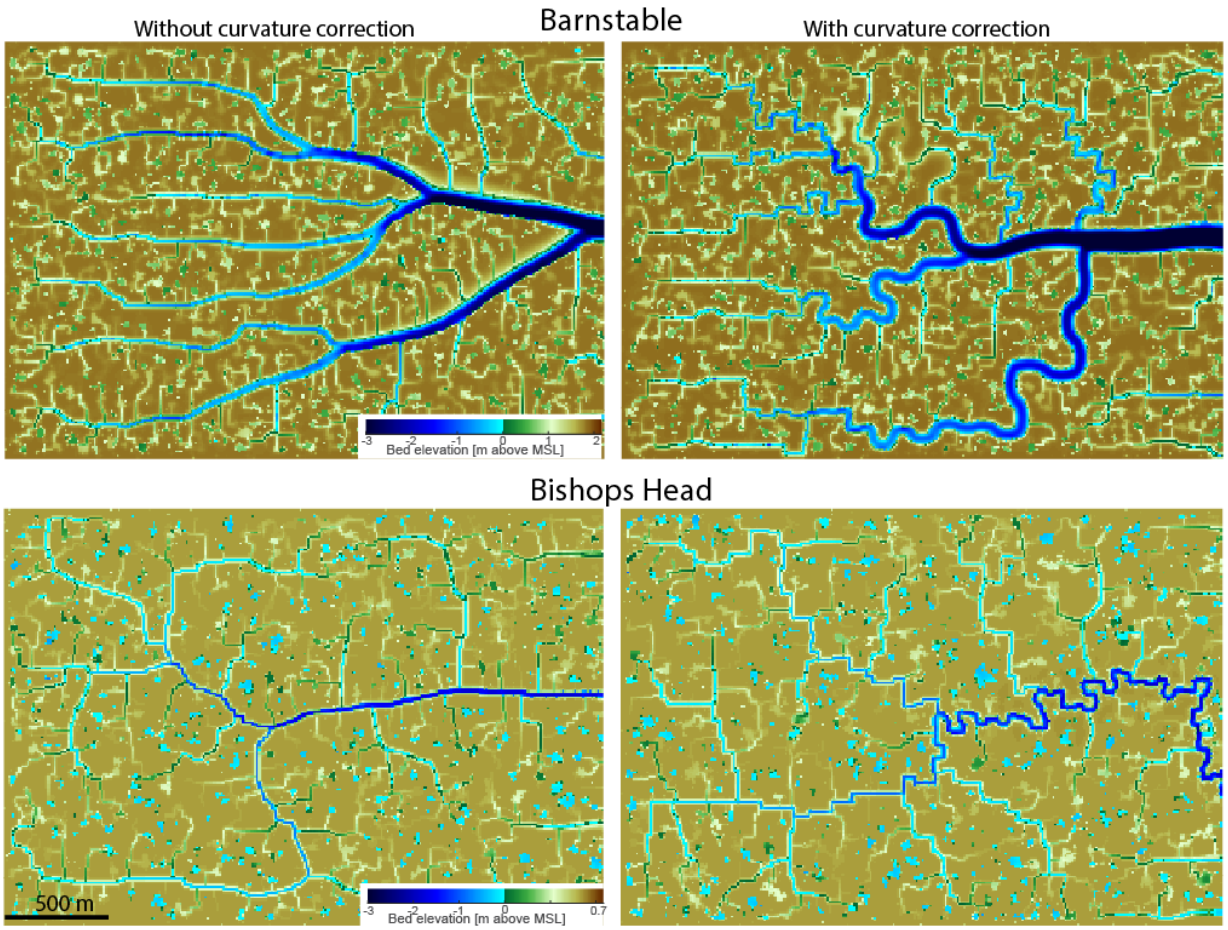

Figure 4. Comparison of numerically modeled topobathymetry with and without the curvature-driven flow modification, at t=3000 yr, for the reference simulation (k=0.2, dx=10 m). The domain is the same as the red rectangle in Fig. 1.

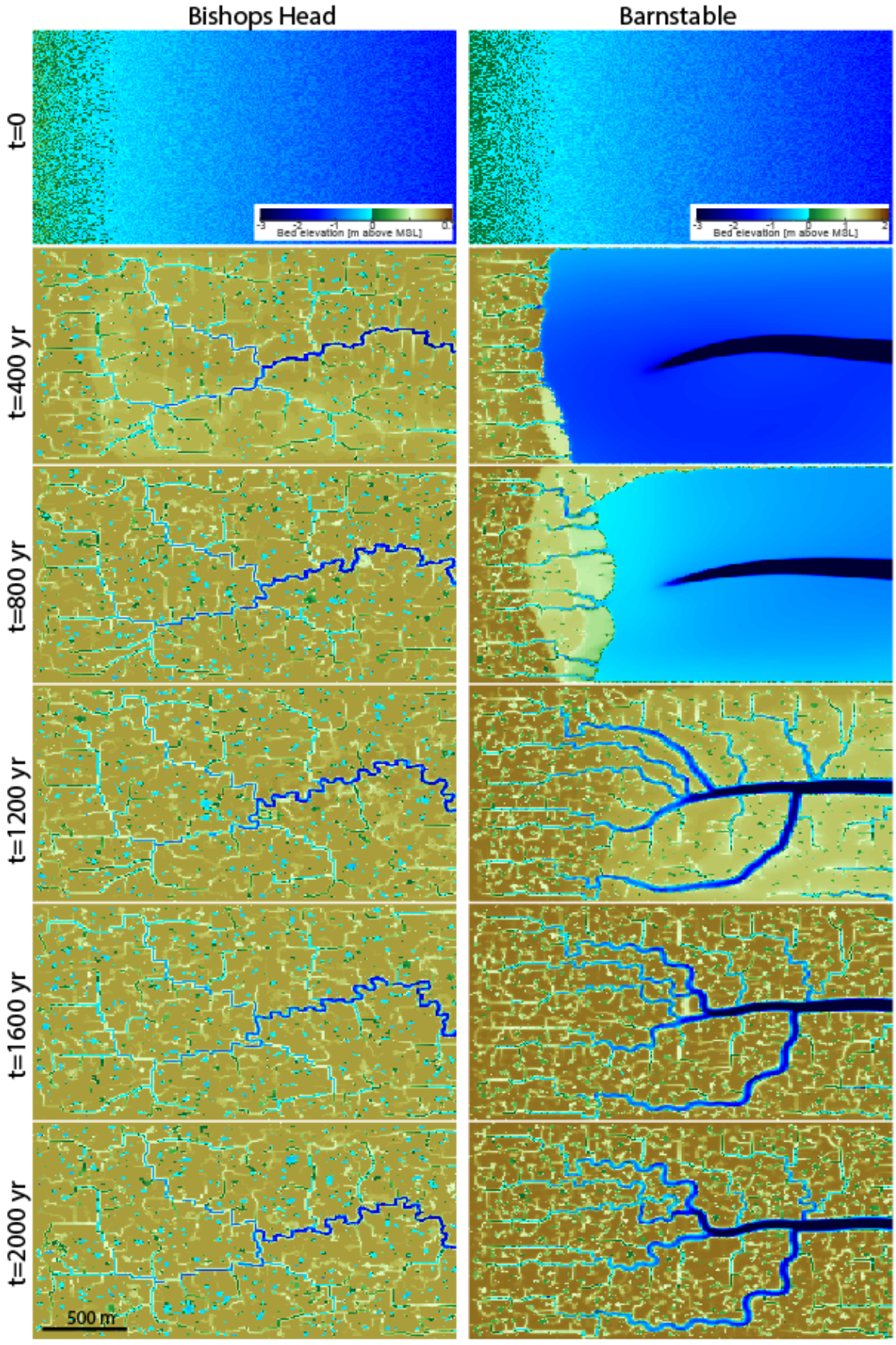
Bishops Head
Barnstable
t=0
t=400 yr
t=800 yr
t=1200 yr
t=1600 yr
t=2000 yr
Bed elevation [m above MSL]
Bed elevation [m above MSL]
500 m

Figure 5. Numerically modeled topobathymetry at different times for the reference simulation (k=0.2, dx=10 m) in the case of Bishops Head and Barnstable. Note that channel sinuosity increases over time. The domain is the same as the red rectangle in Fig. 1.

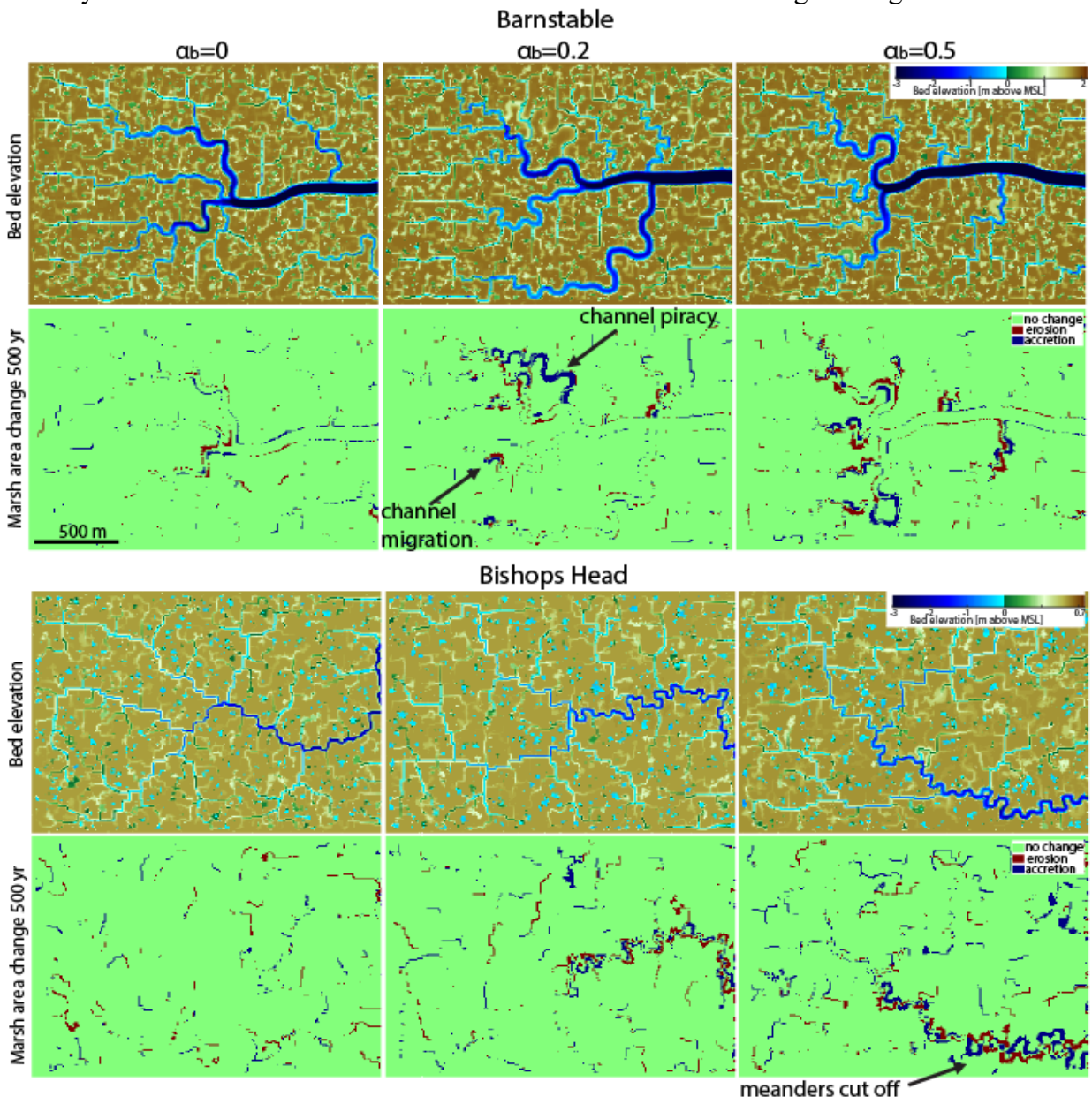

Figure 6: Comparison of simulated topobathymetry at t=3000 yr for different values of the bank erodibility coefficient k. The resolution of the computational grid dx=10 m is fixed for all the simulations. The Barnstable case with k=0.2 shows an instance of channel piracy, where the abandoned channel is quickly filling in (colored blue in the panel showing the marsh area change).

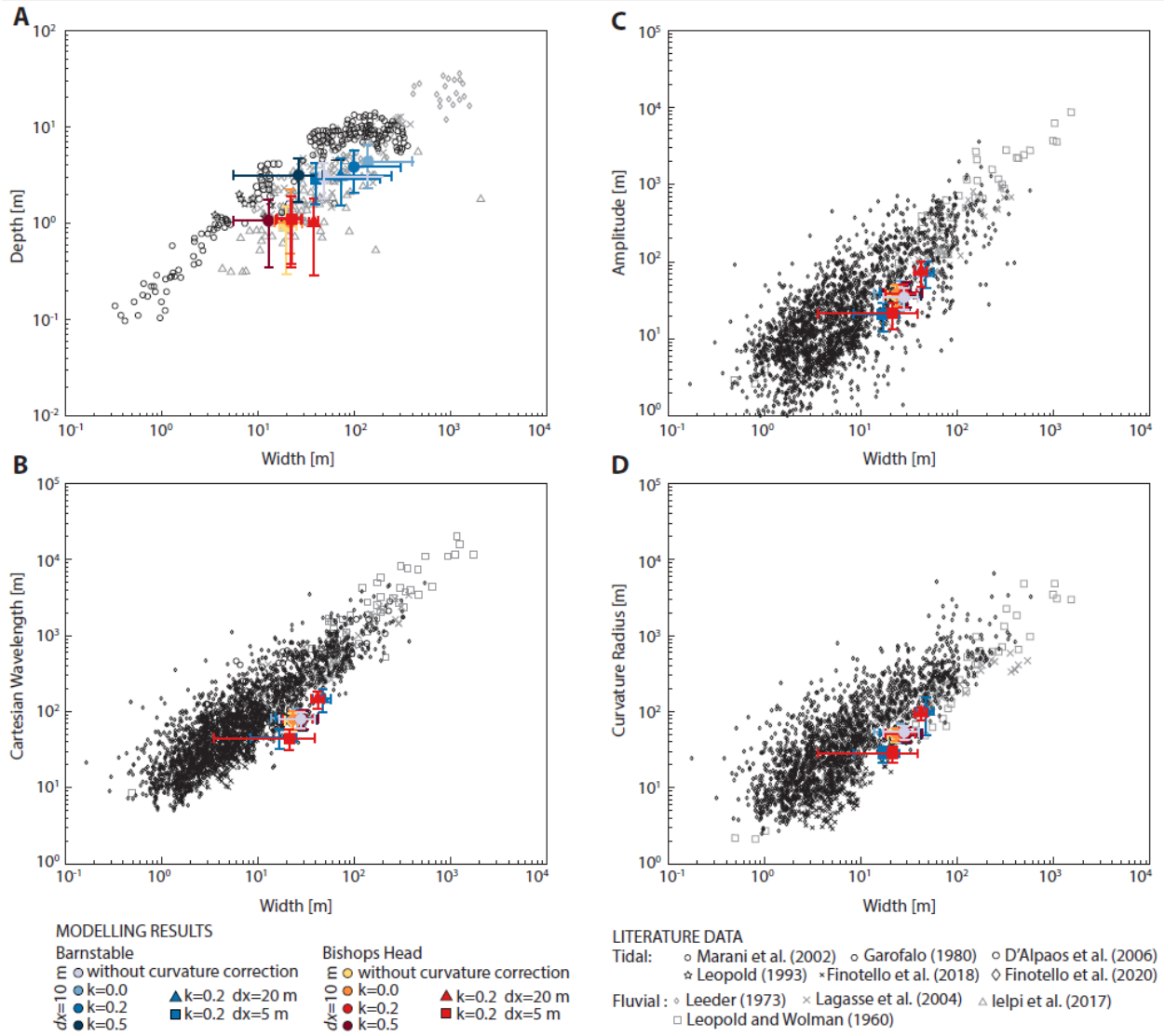

Figure 7: Comparison between planform features of modeled tidal meanders with field data retrieved from the literaure. Modeling results are reported as average ensemble data for individual simulations performed using different model parameters at both the Barnstable and Bishops Head study sites, with error bars indicating standard deviation. In agreement with the literature data, panel A show data referring to entire tidal meandering channels, whereas the other panels display morphometric data specific to individual meander bends.

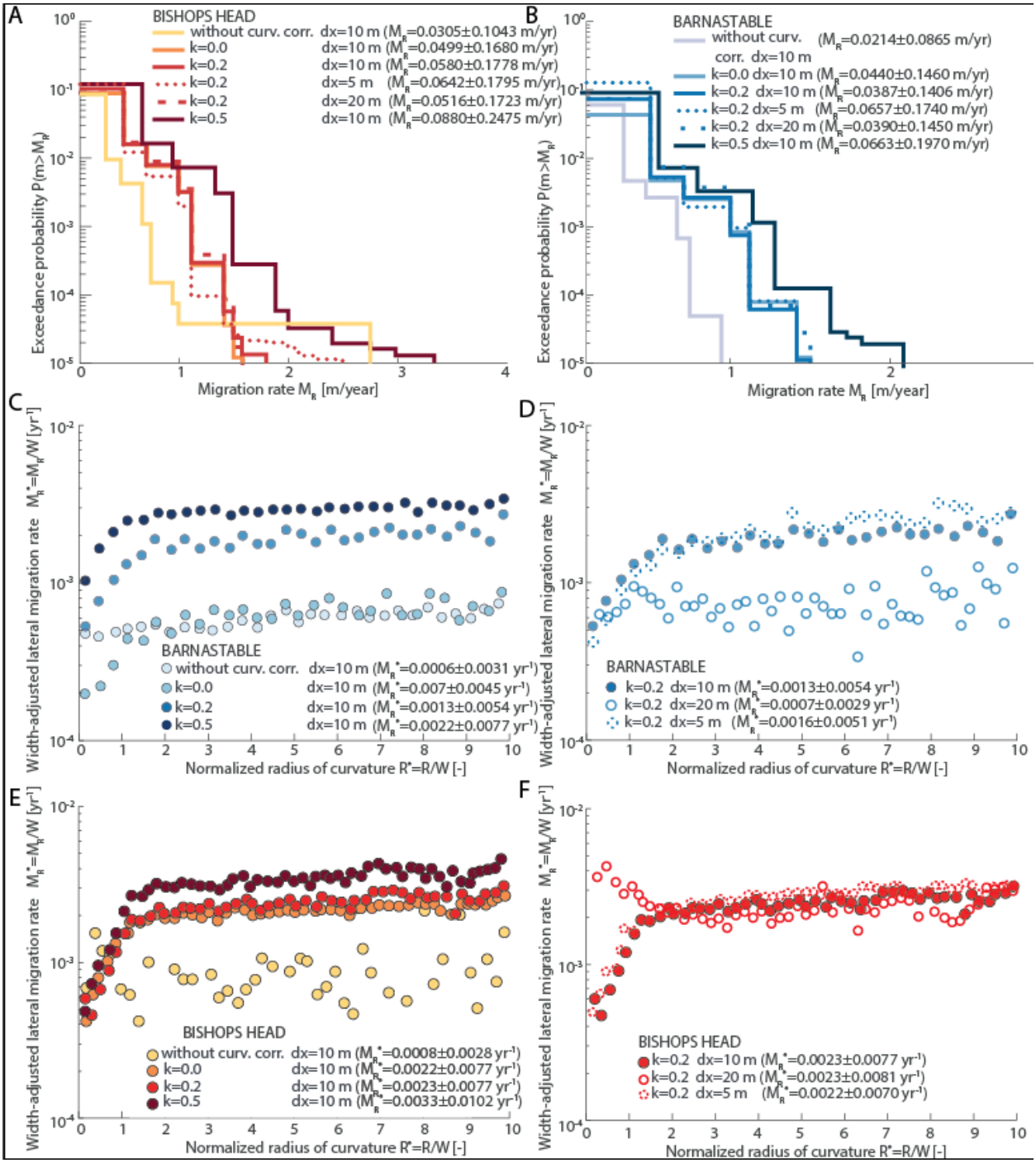

Figure 8: Characteristics of numerically modeled tidal meanders. A,B) Empirical probability distributions of numerically modelled meander migration rates M_R. C,D,E,F) Width-adjusted migration rates ($M_R^* = M_R/W$) plotted against the normalized meander radius of curvature ($R^* = R/W$), with dots representing the binned median values of the M_R^* distirbution obtained by binning together a set of n data points equal to 100 and 50 for Barnstable and Bishops Head, respectively. In each panel, different marker/line color correspond to different simulations, with the parameters employed in each simulations reported in the legends.

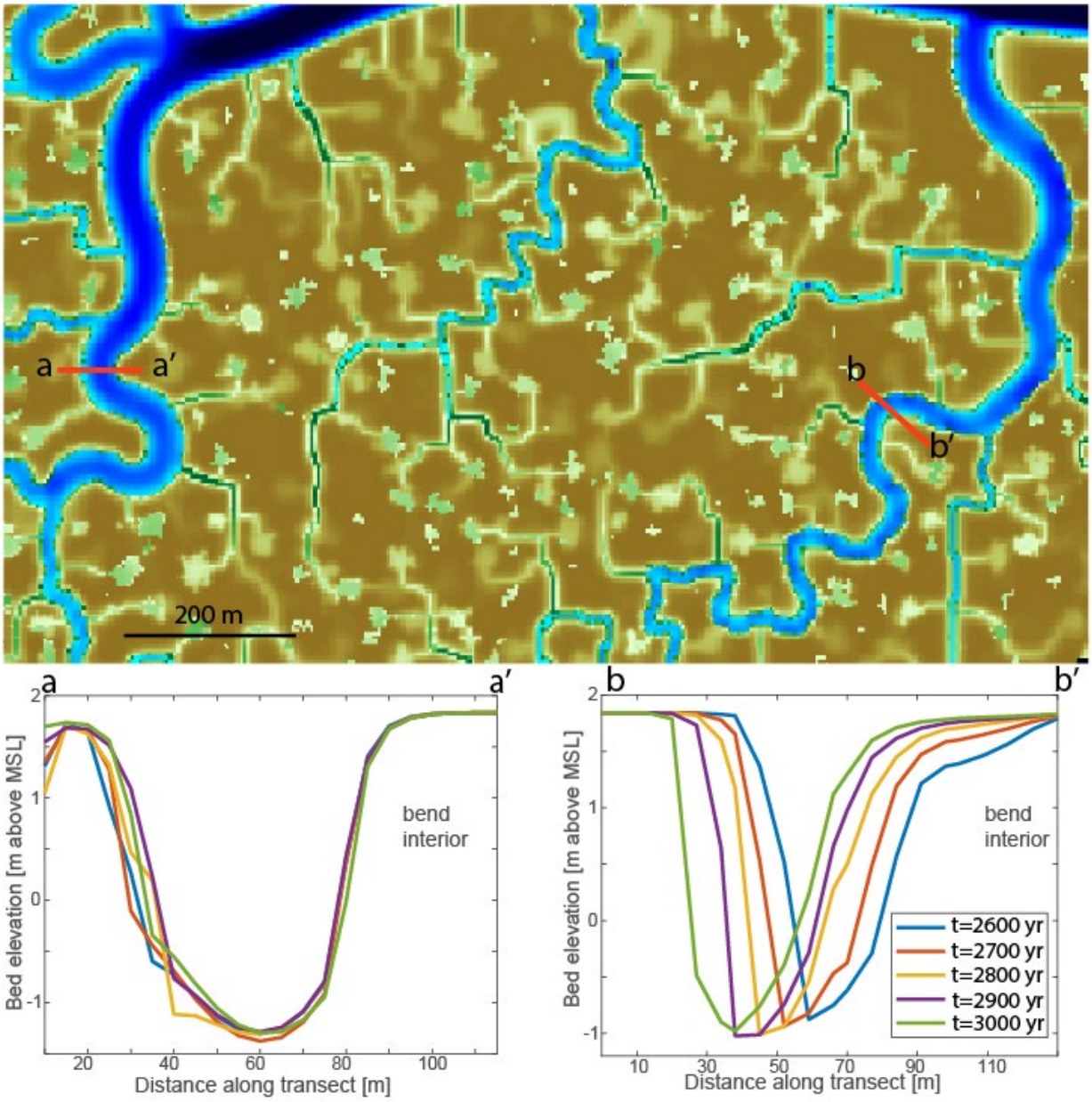

Figure 9: Details of channel migration at two bends, for the Barnstable case with dx=5 m, at t=3000 yr (as in Fig. 11). Transect a-a' shows an example of a cuspate channel, where the thalweg is shifted toward the interior of the bend.

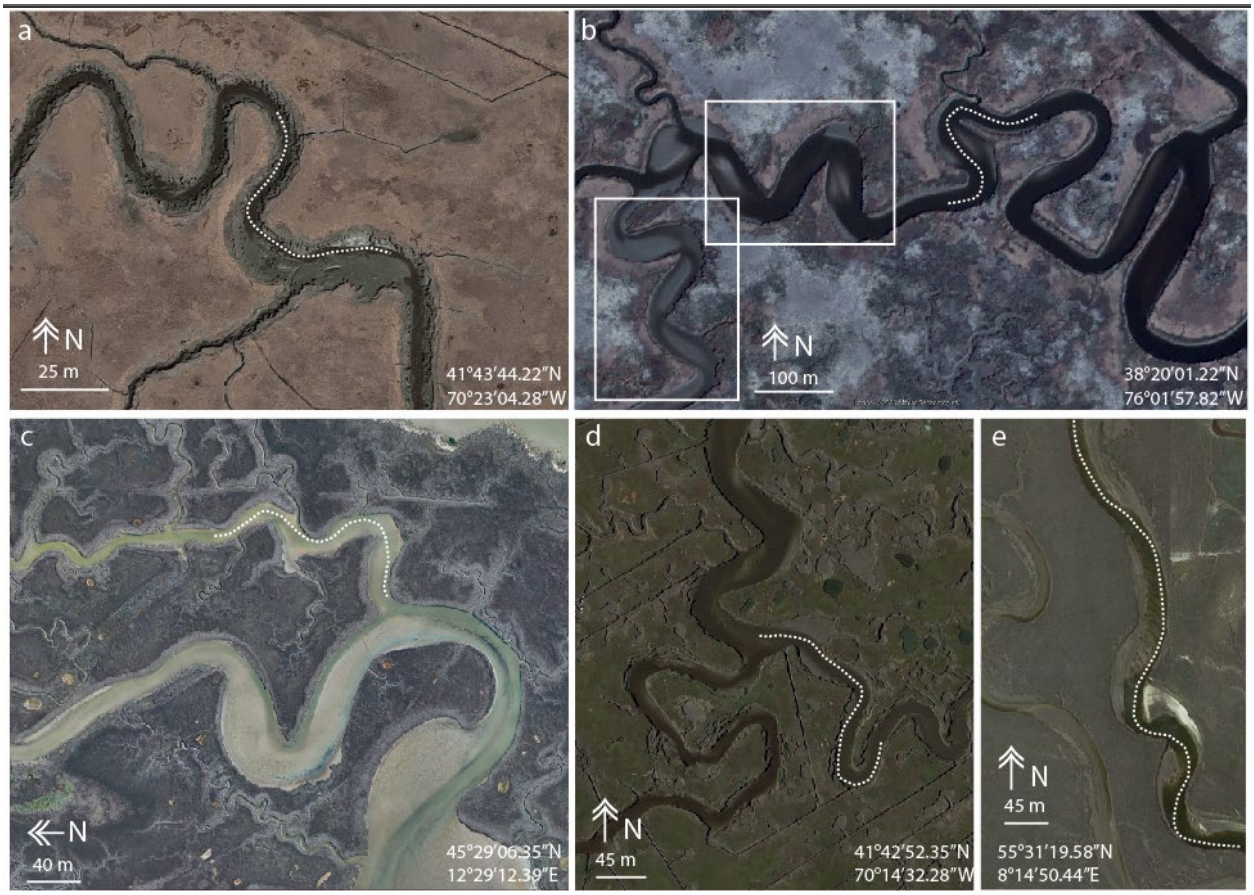

Figure 10: Examples of tidal meandering channels whose thalweg is not located at the outer bank. A) Barnstable Great Marshes, MA, USA (Image©Google, Landsat); B) Bishops Head, MD, USA (Image©Google, Maxar Technologies); C) Venice Lagoon, Italy (Image©Google, Landsat); D) Barnstable Great Marshes, MA, USA (Image©Google, Landsat); E) Skallingen Peninsula, Denmark (Image©Google, Landsat). The approximate thalweg position is denoted by dashed lines. Rectangles in panel B denote segregated ebb and flood channels.

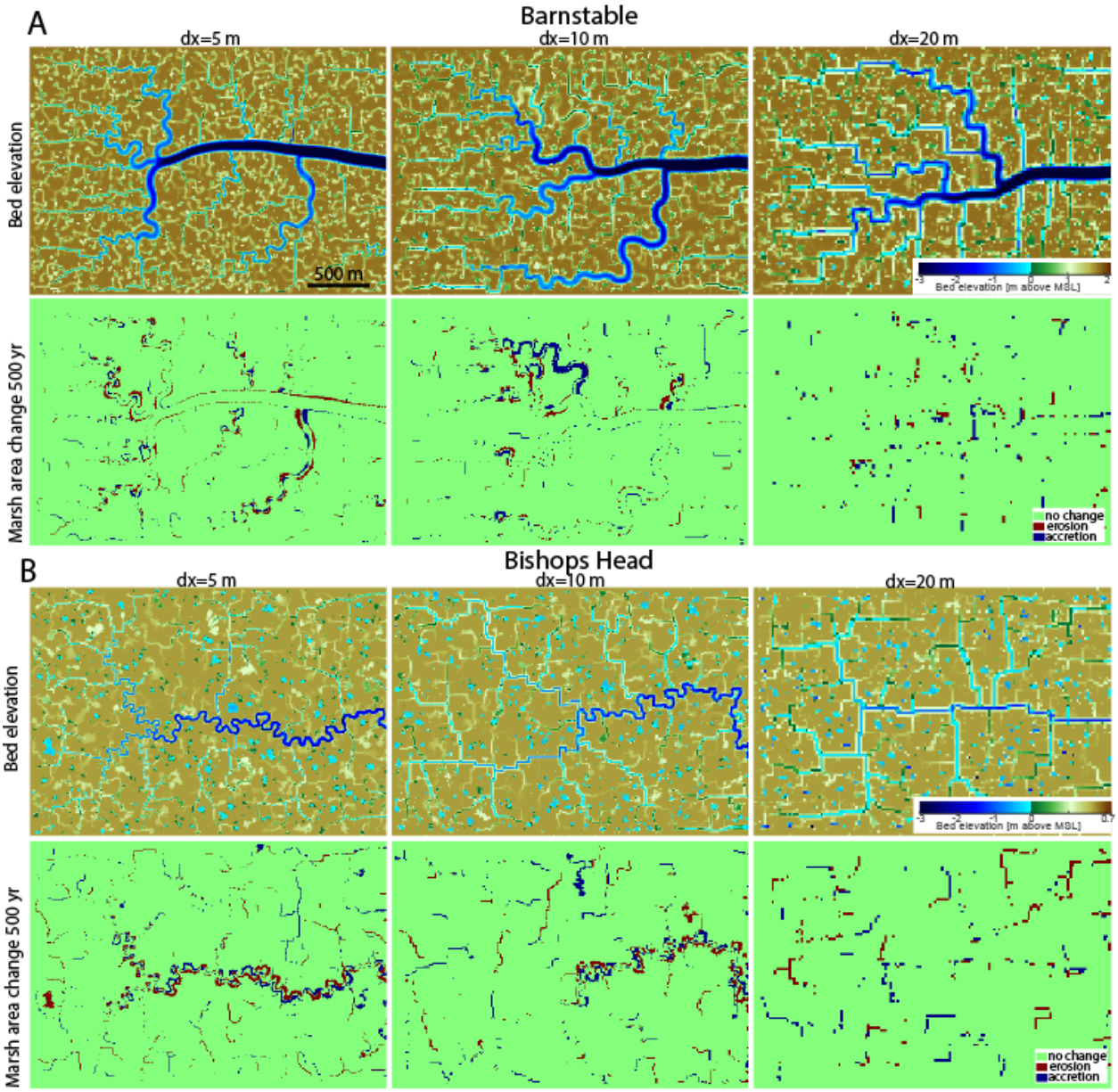

Figure 11: Comparison of simulated topobathymetry at t=3000 yr for different grid resolutions (*dx*) with the standard bank erodibility (*k*=0.2).

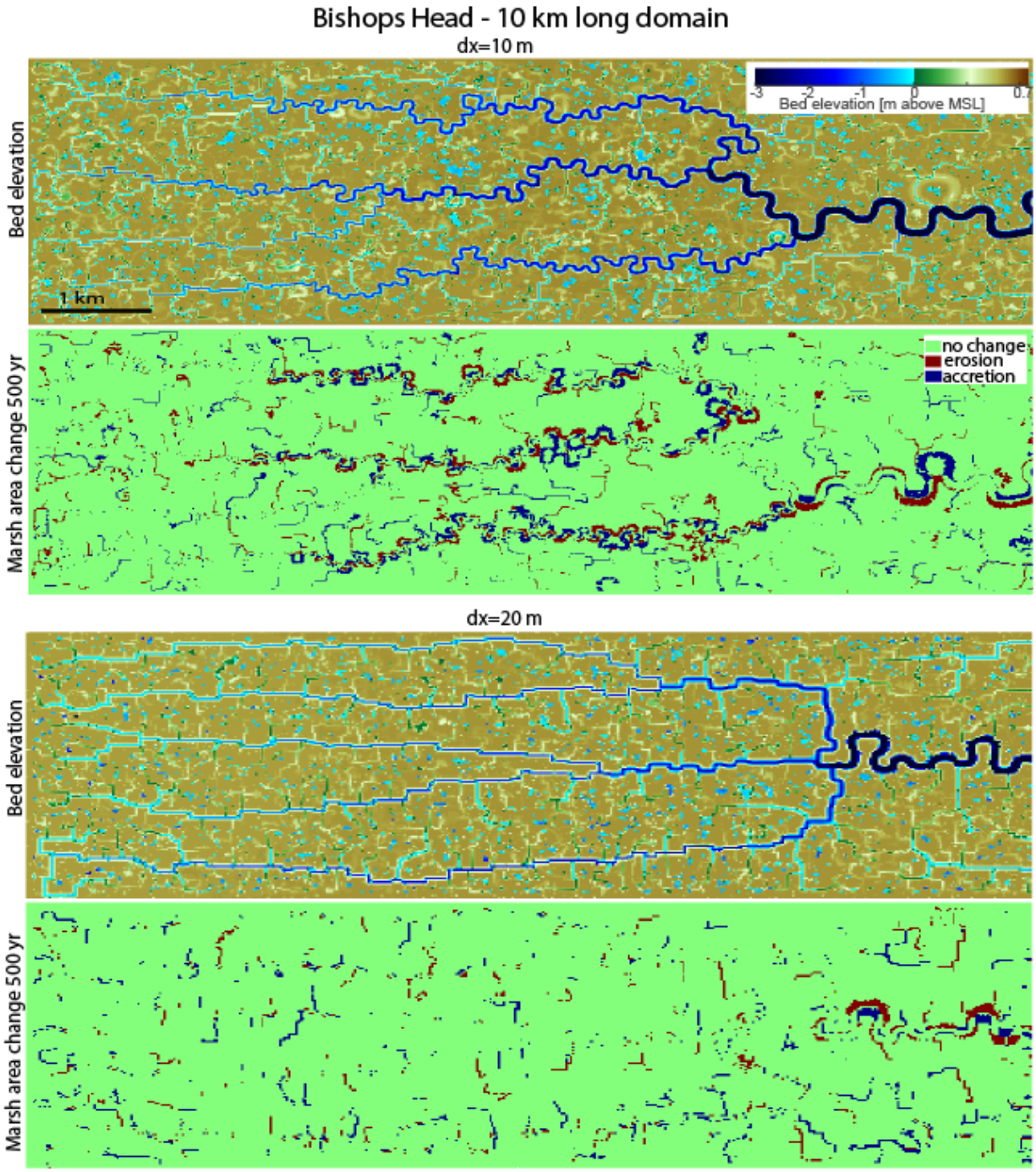

Figure 12: Comparison of simulated topobathymetry for Bishops Head at t=3000 yr for different grid resolutions (dx), with the standard bank erodibility (k=0.2). The domain is 10 km long instead of 3 km long (as in all other simulations).

Supporting Information for

A flow-curvature-based model for channel meandering in tidal marshes

Giulio Mariotti[1,2,*] and Alvise Finotello[3]

[1]Department of Oceanography and Coastal Sciences, Louisiana State University, Baton Rouge, LA, USA
[2]Center for Computation and Technology, Louisiana State University, Baton Rouge, LA, USA
[3]Department of Geosciences, University of Padova, Padova, Italy.

*Corresponding author: Giulio Mariotti (gmariotti@lsu.edu)

Contents of this file

Analysis of the numerical simulations to quantify morphometric characteristics and planform dynamics

The first step involved deriving the topology of the tidal channel network. The latter was analyzed using a fixed time-interval Δt=20 years to allow for significant morphological changes. Therefore, a binary mask was created at every Δt to distinguish between the active flow domain (i.e., tidal channels and tidal flats) and the adjacent vegetated marsh platform. The analysis focused on mature tidal channel networks and therefore began when the position of the seaward marsh edge became fixed. This occurred at approximately t=600 years at Bishops Head and t=1200 years at Barnstable. Once the binary mask was obtained, the centerline of the tidal channel network was determined through a standard skeletonization procedure. Additionally, the width of each centerline pixel (W_i [m]) was calculated through the Euclidean distance transform applied to the original binary image.

Subsequently, the skeletonize network was segmented into individual branches by filtering out branchpoint pixels (i.e., confluences or bifurcations). For each individual branch, local channel curvature was computed as $C = -d\theta/ds$ ([m^{-1}]), where θ is the angle formed by the channel axis and the horizontal direction, and s is the intrinsic (i.e., along-channel) coordinate assumed to be positive in the landward direction (Finotello et al., 2020a; Marani et al., 2002). Individual network branches comprising less than 5 pixels and/or having a mean width lower than 1.5 pixels were excluded from the analysis.

Curvature computation allowed for the identification of individual meander bends, defined as channel portions included between two consecutive inflection points (i.e., pixels where $C = 0$). Meander apexes were also identified as points corresponding to local maxima of curvature. The morphological features of individual meander bends were characterized using various morphometric parameters: the average channel width (W [m]) and depth (D [m]), the latter being computed as the bankfull depth with reference to the marsh elevation; the meander intrinsic wavelength (ℓ [m]), which represents the along-channel distance along meander inflection points; the meander Cartesian wavelength (L [m]), defined as the planar distance between meander inflections; the meander sinuosity (χ [-]), calculated as $\chi=\ell/L$; the meander amplitude (A [m]), measured as the maximum point-line distance between any centerline point and the line connecting the two meander flexes; the meander radius (R [m]), which is the radius of the best-fitting circle obtained by considering all meander centerline points; and the meander asymmetry index $\mathcal{A} = (\ell_u - \ell_d)/\ell$ ([-]), where ℓ_u and ℓ_d denote the distances between the meander apex and its upstream and downstream flexes, respectively.

Channel lateral migration was computed by comparing pairs of consecutive skeletonized networks and then relating locations of individual channel points through a distance-based searching algorithm. Specifically, we associated each i pixel in the initial network with its nearest j pixel in the final network using a nearest-neighbour algorithm and computing the centerline migration rate as $M_R = \Delta t/\Delta_{ij}$ ([m/yr]), where Δ_{ij} ([m]) denotes the distance between i and j. Although typical proximity algorithms (such as nearest neighbor and inverse distance weighted) can at times result in large gaps between correlated points (see Sylvester et al., 2019), they are computationally efficient and allow

for automatic computation of lateral channel migration even within complex tidal channel networks. Notably, analyses of migration rates were restricted to channels larger than one and a half computational cells. This filtering was implemented to eliminate spurious results stemming from the model's limited ability to accurately simulate meandering within narrower channels. Moreover, meander cutoffs and channel piracy events, which significantly modify network topology and would result in unrealistically high migration rates, were filtered out based on structural similarity index measure (SSIM) computed for pairs of binary masks and discarding pixels whose SSIM exceeds the critical 0.1 thresholds.

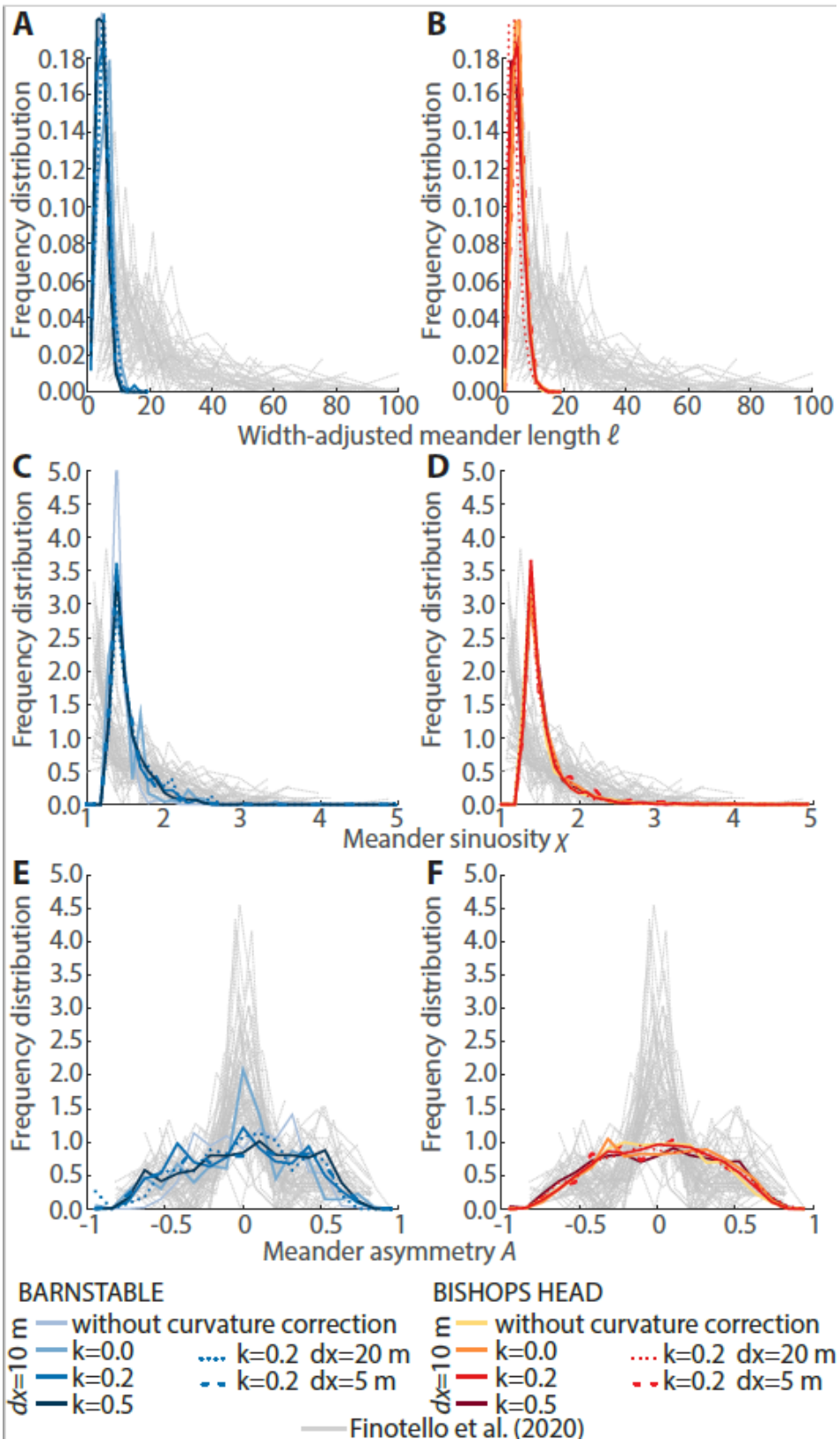

Figure S1. Frequency distributions of dimensionless meander morphometric variables. (a,b) width-adjusted meander intrinsic length; (c,d) meander sinuosity; (e,f) meander

asymmetry index. Modeling results are presented as probability distributions obtained by considering the orphologies of meandering channels at the final time step of the numerical simulations at both the Barnstable (blueish colors) and Bishops Head (reddish colors) study sites. Different colors and line styles denote different numerical simulations. Gray lines in the background represent literature data on tidal meandering channels derived from Finotello et. al (2020).

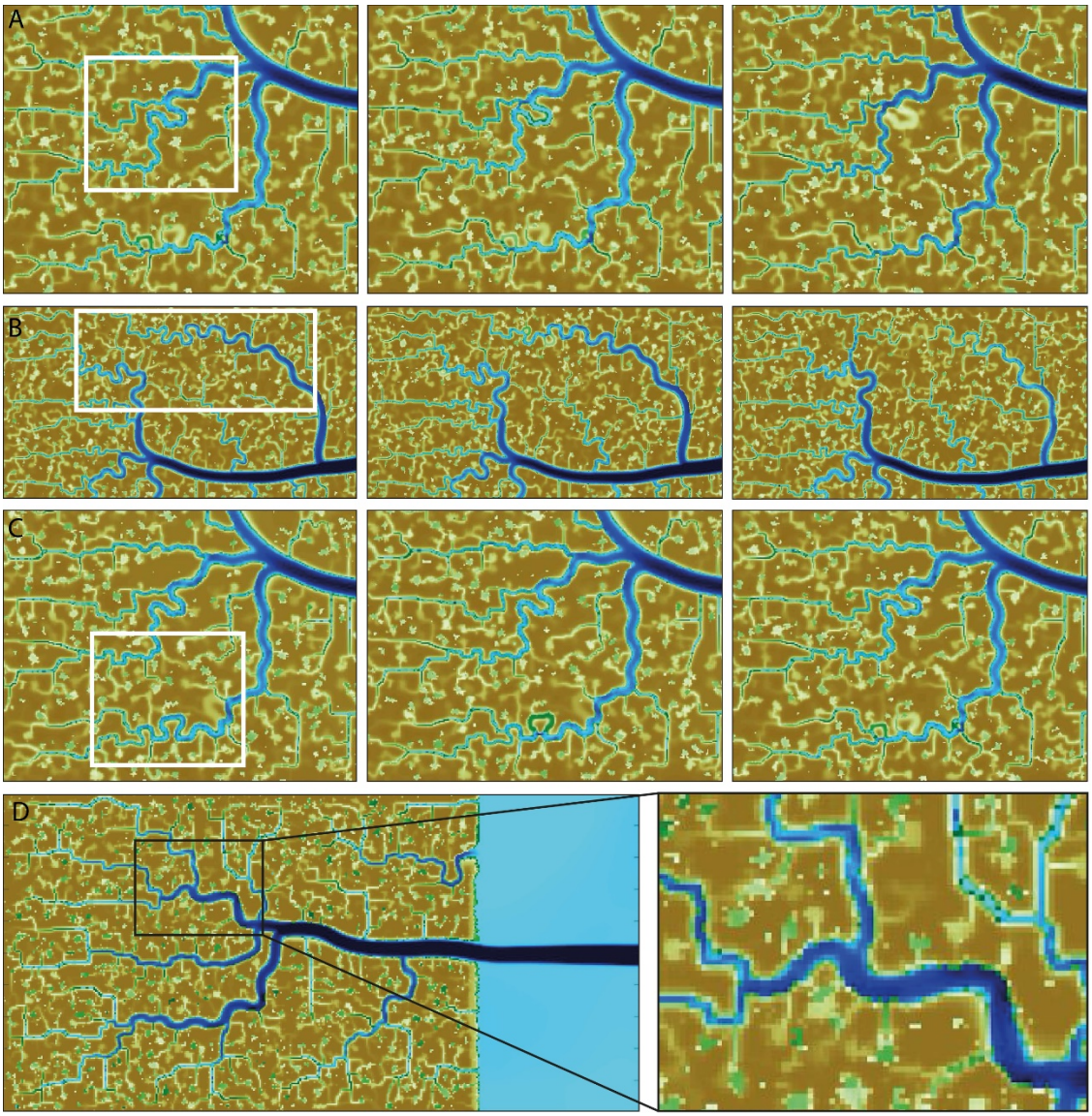

Figure S2. Examples of inter- and intra-channel dynamics and peculiar meander morphologies induced by stream meandering in the numerical simulations representing the Barnstable study case. A) Channel piracy forming a morphology akin to a meander cutoff. B) Repeated meander cutoffs and piracy resulting in a network reorganization. C) Meander Cutoffs. D) Meander bends with cuspate inner banks. Rectangles highlight the area of interest.

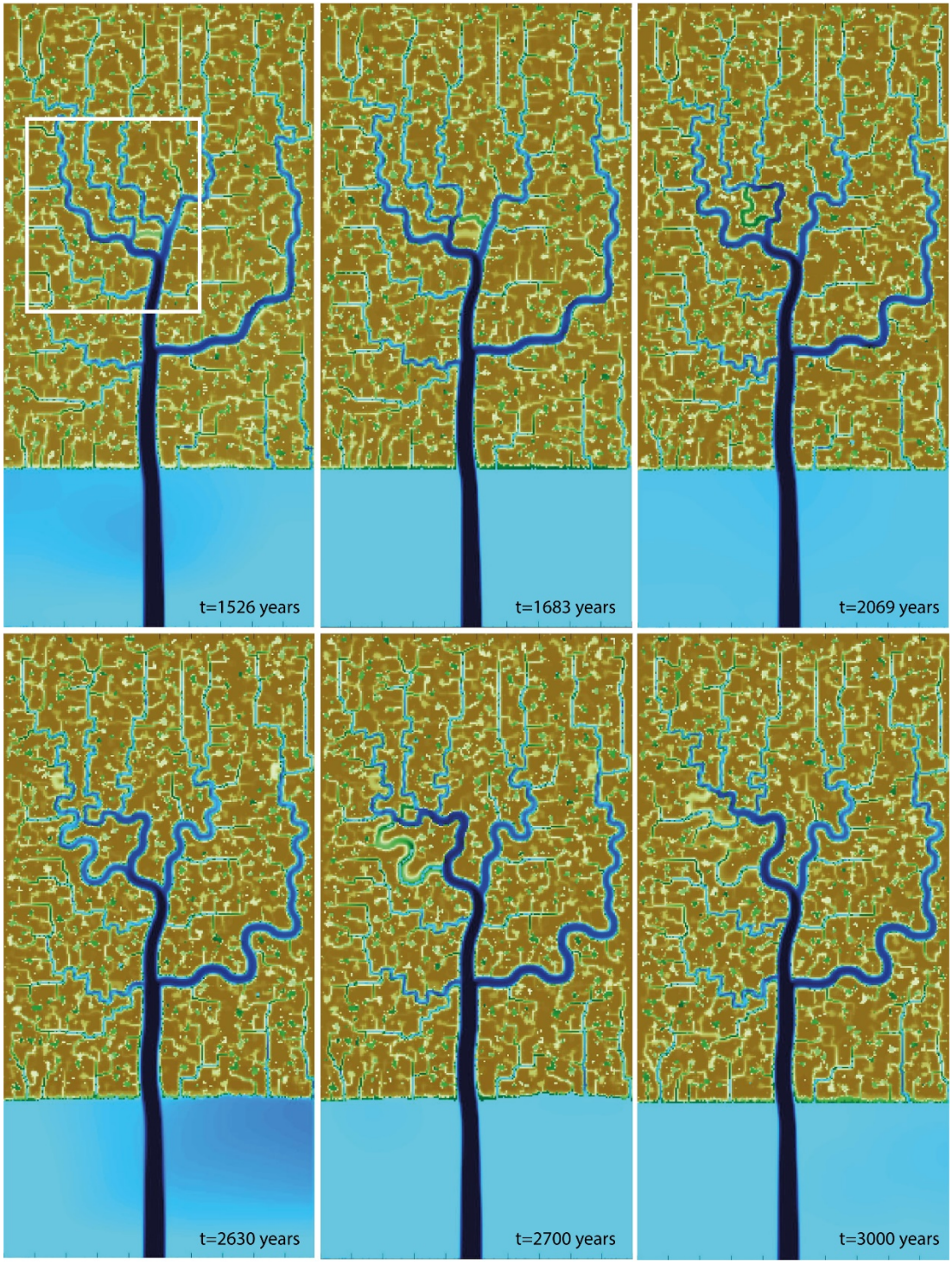

Figure S3. Examples of inter- and intra-channel dynamics (i.e., meander cutoffs and channel piracies) resulting in repeated network reorganizations in the numerical simulations for the Barnstable marsh.

Figure S4. Example of channel cutoff and piracies from the Seabrook-Hamptons Estuary (NH, USA) (Image ©Google, Landsat/Copernicus).

List of videos

Video BARNSTABLE_k0_dx10. Simulation for Barnstable marsh, with dx=10 and k=0.
Video BARNSTABLE_k02_dx10. Simulation for Barnstable marsh, with dx=10 and k=0.2
Video BARNSTABLE_k05_dx10. Simulation for Barnstable marsh, with dx=10 and k=0.5.
Video BARNSTABLE_k02_dx5. Simulation for Barnstable marsh, with dx=5 and k=0.2.
Video BARNSTABLE_k02_dx20. Simulation for Barnstable marsh, with dx=20 and k=0.2.

Video BISHOPS _k0_dx10. Simulation for Bishops Head marsh, with dx=10 and k=0.
Video BISHOPS_k02_dx10. Simulation for Bishops Head marsh, with dx=10 and k=0.2
Video BISHOPS_k05_dx10. Simulation for Bishops Head marsh, with dx=10 and k=0.5.
Video BISHOPS_k02_dx5. Simulation for Bishops Head marsh, with dx=5 and k=0.2.
Video BISHOPS_k02_dx20. Simulation for Bishops Head marsh, with dx=20 and k=0.2.

Video longBISHOPS_k0_dx10. Simulation for Bishops Head marsh with a long domain (as in Figure 12), with dx=10 and k=0.
Video longBISHOPS_k02_dx20. Simulation for Bishops Head marsh with a long domain (as in Figure 12), with dx=20 and k=0.2